Dynamics of shallow hydrothermal eruptions: new insights from the Vulcano's Breccia di Commenda eruption

Mauro Rosi[1], Federico Di Traglia[2]*, Marco Pistolesi[1], Tomaso Esposti Ongaro[3], Mattia de' Michieli Vitturi[3], Costanza Bonadonna[4]

1) Dipartimento di Scienze della Terra, Università di Pisa, Via Santa Maria 53, 56126, Pisa, Italy
2) Dipartimento di Scienze della Terra, Università degli Studi di Firenze, Via La Pira 4, 50121, Firenze, Italy
3) Istituto Nazionale di Geofisica e Vulcanologia, Sezione di Pisa, Via della Faggiola 32, 56126, Pisa, Italy
4) Département des Sciences de la Terre, Université de Genève, Rue des Maraîchers 13, CH-1205, Geneva, Suisse

*corresponding author: Federico Di Traglia, Dipartimento di Scienze della Terra, Università degli Studi di Firenze, Via La Pira 4, 50121, Firenze, Italy, mail to: federico.ditraglia@unifi.it

Abstract

Understanding the dynamics and effects of hydrothermal eruptions is crucial to the hazard assessment in both volcanic and geothermal areas. Eruptions from hydrothermal centers may occur associated with magmatic phases, but also as isolated events without magmatic input, with the most recent examples being those of Te Maari (Tongariro, New Zealand) in 2012 and Ontake (Japan) in 2014. The most recent caldera of the Island of Vulcano (southern Italy) hosts in its center the La Fossa cone, active since 5.5 ka and now characterized by continuous fumarolic degassing. In historical times La Fossa cone has experienced several hydrothermal eruptions, with the most violent event being the Breccia di Commenda eruption, that occurred during the 13th century AD. Based on analysis of 170 stratigraphic logs, we show that the Breccia di Commenda eruption occurred in three main phases. After an opening, low-intensity ash emission phase (Phase 1), the eruption energy climaxed during Phase 2, when a series of violent explosions produced an asymmetric shower of ballistic blocks and the contemporaneous emplacement of highly dispersed, lithic-rich, blast-like pyroclastic density currents (PDCs). The tephra units emplaced during Phase 2, ranging in volume from 0.2 to 2.7 × 10^5 m^3, were covered in turn by thin ash fall deposits (Phase 3). The dynamics of the most violent and intense stage of the eruption (Phase 2) was investigated by numerical simulations. A three-dimensional numerical model was applied, describing the eruptive mixture as a Eulerian-Eulerian, two-phase, non-equilibrium gas-particle fluid (plus a one-way coupled Lagrangian ballistic block fraction). At the initial simulation time, a mass of about 10^9 kg, with initial overpressure above 10 MPa, and a temperature of 250°C, was suddenly ejected from a 200-m-long, eastward inclined, NNE-SSW trending fissure. The mass release formed blast-like PDCs on both sides of the fissure and launched ballistic blocks eastwards. Field investigations and numerical simulations confirm that hydrothermal explosions at La Fossa cone includes intense ballistic fallout of blocks, emission of PDCs potentially travelling beyond the La Fossa caldera, and significant ash fallout. The hazard associated with both ballistic impact and PDC ingress, as associated with hydrothermal eruption, is significantly larger with respect to that associated with Vulcanian-type events of La Fossa.

Keywords

Hydrothermal eruption dynamics

Pyroclastic Density Currents hazard

Volcano ballistic hazard

3D numerical modelling

Island of Vulcano

Introduction and rationale for the study

Phreatic eruptions result when heated groundwater is the driving fluid (Barberi et al. 1992; Germanovich and Lowell 1995; Strehlow et al. 2017), and hydrothermal events occur, when fluids from a pre-existing hydrothermal system are thought to be involved (Marini et al. 1993; Mastin 1995; Browne and Lawless 2001). Such eruptions are typically lithic-rich, and understanding their dynamics is crucial in assessing hazard in active volcanic and geothermal areas (Montalto 1995; Stix and de Moor 2018). These eruptions may occur as isolated events (Le Guern 1980; Sheridan 1980; Marini et al. 1993; Yamamoto et al. 1999; Ohba et al. 2007; Fujinawa et al. 2008; Houghton et al. 2011; Miura et al. 2012; Montanaro et al. 2016a,b; Mannen et al. 2018) or may be associated with magmatic phases (Chrétien and Brousse 1989; Calvache and Williams 1992; Gardner and White 2002). In the latter case there may be precursory activity, on the former there may not (Barberi et al. 1992; Strehlow et al. 2017). Recent events of the isolated (phreatic event at a hydrothermal system) category have occurred at Te Maari craters (Tongariro volcanic complex; New Zealand) in August 2012 (Lube et al. 2014) and at Ontake volcano (Japan) in September 2014 (Oikawa et al. 2016). During the Ontake event, 64 climbers lost their life (Tsunematsu et al. 2016), demonstrating the potential hazard presented by this type of volcanic phenomenon which involves a sudden explosion with little (to no) warning. Worldwide, active volcanoes in a quiescent state often attract large numbers of tourists crowding active degassing areas overlying very-active hydrothermal systems (Heggie 2009; Erfurt-Cooper 2011). Phreatic/hydrothermal explosive events can occur with little or no precursors (e.g., Chrétien and Brousse 1989; Hurst et al. 2014; Kato et al. 2016) and can generate lethal phenomena such as intense showers of blocks and highly energetic pyroclastic density currents (PDCs; e.g., Sheridan and Malin 1983; Fitzgerald et al. 2014; Tenaka et al. 2018). Volcanologists, therefore, need to understand better the processes that drive their occurrence and to accurately assess their hazards (e.g., Barberi et al. 1992; Hincks et al. 2014; Fitzgerald et al. 2017).

The Island of Vulcano (Aeolian Archipelago), located in southern Italy (Fig. 1), hosts in its northern part a caldera (Gioncada and Sbrana 1991; Ventura 1994, Ventura et al. 1999; Ruch et al. 2016).

78 Activity has been concentrated in the last 5000 years at La Fossa cone and at Vulcanello peninsula
79 (Frazzetta et al. 1984; De Astis et al. 2013; Fusillo et al. 2015). The La Fossa caldera is characterized
80 by large-scale degassing phenomena, most of which occurs through high-temperature fumaroles
81 within the summit crater of the cone (occasionally up to more than 600°C; Chiodini et al. 1995;
82 Granieri et al. 2006; Diliberto 2017), and as widespread soil degassing within the crater and on its
83 flanks which feeds boiling mud pools and underwater degassing manifestations around the harbour
84 area (Chiodini et al. 1996; Capasso et al. 1997; Harris and Stevenson 1997; Federico et al. 2010;
85 Paonita et al. 2013; Capasso et al. 2014; Mandarano et al. 2016). During the summer season, the
86 island hosts up to 20,000 people, with hundreds of tourists climbing every day following marked and
87 maintained trails into the Fossa crater (Biass et al. 2016a). Because La Fossa cone experienced a
88 lithic-rich eruption (the Breccia di Commenda event) during the 13th century AD (Gurioli et al. 2012),
89 and other similar events likely occurred in 1444 and in 1727 AD from vents opening on the northern
90 flank and at the summit of the cone (Mercalli and Silvestri 1891; De Fiore 1922; Frazzetta et al. 1983;
91 Di Traglia et al. 2013), the study of these events is particularly relevant for risk assessment and crisis
92 management in a highly visited and populated volcanic setting.
93 The present study thus follows up on that of Gurioli et al. (2012) in its aim to more fully understand
94 the physical and sedimentological processes that occurred during the Breccia di Commenda event.
95 This is achieved through the integration of detailed field and laboratory analyses of deposits, as well
96 as numerical modelling of PDCs and ballistic blocks dispersal of the most energetic phase during the
97 eruption. Assessment of the physical volcanology of the Breccia di Commenda event, and a
98 comparison with similar events that occurred at volcanoes with active hydrothermal systems (e.g.,
99 Sheridan 1980; Lube et al. 2014; Oikawa et al. 2016) also highlights similarities in terms of timing,
100 eruptive mechanisms and energy release between geographically diverse, but process-similar,
101 systems across the globe.
102
103 **Geological and volcanological background**

104 The Island of Vulcano consists of six volcanic edifices whose formation overlapped in time and space
105 beginning 120 ka (Keller 1980; De Astis et al. 2013). The northern part of the island (Fig. 1) hosts a
106 4 × 2 km caldera structure (La Fossa Caldera; Gioncada and Sbrana 1991; Ventura 1994, Ventura et
107 al. 1999; Romagnoli et al. 2015; Ruch et al. 2016) whose borders are exposed in the southern and
108 western sectors. In historical times, volcanic activity has occurred at two centers within the caldera:
109 at La Fossa cone, that began to erupt 5.5 ka and which is located almost in the centre of the caldera
110 (Frazzetta et al. 1984; De Astis et al. 2013) (Fig. 1), and at the Vulcanello islets, located along the
111 northernmost border of the caldera. The Vulcanello vent was likely active both in Roman time
112 (Mercalli and Silvestri 1891; De Fiore 1922) and between the 11^{th} and 17^{th} centuries AD (Arrighi et
113 al. 2006; Davì et al. 2009a; Fusillo et al. 2015). Magmatic eruptions at Vulcano Island are related to
114 the ascent of deep basic (basaltic/shoshonitic) magmas that trigger episodes of recharge and mixing
115 toward the upper magmatic reservoirs (Nicotra et al. 2018). The recent eruptive activity (<2 ka)
116 appears to have been also controlled by the activity of the N-S trending, regional fault (Ventura 1994,
117 Ventura et al. 1999; Ruch et al. 2016).
118
119 *The Breccia di Commenda eruption*
120 Several previous studies have addressed the Breccia di Commenda deposits, which was referred to
121 as the Breccia di Commenda in Gurioli et al. (2012), as Commenda Eruptive Unit in Di Traglia et al.
122 (2013), or as Caruggi formation in Dellino et al. (2011), De Astis et al. (2006), De Astis et al. (2013).
123 Frazzetta et al. (1983) described the Breccia di Commenda (namely "Marker bed Explosion Breccia
124 (EB)") as a phreatic explosive breccia composed of yellow fragments (due to fumarolic alteration)
125 and ranging in composition from trachyte to andesite. Frazzetta et al. (1983) also described the unit
126 as being roughly separated into an ash fall sub-unit scattered around the crater, and a coarse-grained
127 flow sub-unit cropping out near the base of the cone. According to Dellino et al. (2011) and De Astis
128 et al. (2013), this "Caruggi formation" was emplaced around 1250 y BP, and mainly consists of lithic
129 clasts characterized by a high degree of hydrothermal alteration. From deposit base to top, Dellino et

130 al. (2011) and De Astis et al. (2013) recognized an exotic fine ash layer related to the eruption of Mt.
131 Pilato, that occurred in the neighbouring Island of Lipari, a meter-thick layer of dense lapilli and
132 blocks set in an ash matrix, a dense lapilli- and blocks-bearing layer and a final, thinly-laminated ash
133 layer. According to Di Traglia et al. (2013), the Breccia di Commenda eruption was part of the Palizzi-
134 Commenda Eruptive Cluster, which precedes the last eruptive cycle at La Fossa (Gran Cratere
135 eruptive cluster; 1444-1890 AD; Fig. 2a).
136 The Palizzi-Commenda eruptive cluster can, in fact, be divided to a younger unit (Palizzi eruptive
137 unit; 1170±20 AD – 1230±20 AD) followed by the Commenda eruptive unit (Di Traglia et al. 2013).
138 This consists of a lower breccia deposit (Breccia di Commenda, Gurioli et al. 2012; the focus of this
139 study), overlain by a sequence of thinly stratified reddish ash layers (Varicolored Tuffs or "Tufi
140 Varicolori"--in Italian; Frazzetta et al. 1983; Capaccioni and Coniglio 1995; Dellino et al. 2011; Fig.
141 2a). Despite the variability of the nomenclature used in the recent literature to designate the deposits
142 of this event, for the sake of simplicity we have adopted the term “Breccia di Commenda” (hereafter
143 BdC) eruption to refer to the coarse-grained, breccia sequence, and “Tufi Varicolori” to refer to the
144 fine ash sequence on top of it.
145 A relevant feature of the BdC event is represented by its contemporaneity with the explosive eruption
146 of the Rocche Rosse (Cortese et al. 1986; Dellino and La Volpe 1995; Forni et al. 2013), whose vent
147 was located on the Island of Lipari, within the Monte Pilato cone, about 12 km north of the La Fossa
148 crater. The Rocche Rosse eruption was characterized by a first phase of explosive activity (Forni et
149 al. 2013) which culminated with the emplacement of the Rocche Rosse lava flow (Bullock et al. 2018)
150 dated at 1230±20 AD (Arrighi et al. 2006; Fig. 2a). White, fine-grained ash layers with a rhyolite
151 composition (Rocche Rosse tephra; Cortese et al. 1986) are in fact ubiquitously interbedded with the
152 BdC deposits (Gurioli et al. 2012; Di Traglia et al. 2013; Fig. 2b).
153 Both in our reconstruction and in the work of Gurioli et al. (2012) (Table 1), “phase” refers to a stage
154 of the eruption characterized by certain dynamics, whereas “layer” indicates the deposit associated
155 with this phase. Following the reconstruction of Gurioli et al. (2012), during the BdC eruption, 2 ×

10^6 m^3 of lithic-rich deposits were emplaced mainly as PDCs and minor fallout. The material ejected during the initial phase of the eruption (Phase 1) consisted of grey-coloured, altered lithic ash, which was dispersed by a convective plume towards the NW, producing a few mm-thick ash bed rich in mm-size ash pellets (Layer 1). Phase 1 thus represents the opening phase of the BdC eruption, and shortly preceded the deposition on the Island of Vulcano of the first Rocche Rosse rhyolite ash-fall bed (Gurioli et al. 2012). Following the deposition of the Rocche Rosse tephra, the eruption energy suddenly escalated at La Fossa to produce Phase 2. This phase produced a shower of ballistic blocks and the emplacement of lithic-rich, dilute PDC deposits (to form Layers 2a and 2b) mostly towards the S and SE sectors, followed by the emission of a topographically controlled, coarse-grained, dense PDC (Layer 2c). According to rock magnetic measurements, Phase 2 deposits had a deposition temperature of 200–260°C, consistent with their heating by the hydrothermal system present in the La Fossa cone edifice before the BdC eruption (Fulignati et al. 1998; Gurioli et al. 2012). Phase 2 was closed by the emplacement of Layer 2d, whose deposits consist of 5–10 cm-thick lenses of brown-yellow, massive, well-sorted coarse ash (Gurioli et al. 2012). The eruption ended with a long-lasting emission of ash and with the emplacement of "wet" ash fall deposits (Phase 3), in which non-structured accretionary lapilli are often preserved.

According to Gurioli et al. (2012), the presence of non-vesicular juvenile fragments (20% to 40% by volume) in the deposits, varying in composition from rhyolite to trachyandesite, can be interpreted as indicative of the involvement of juvenile magma. This interacted during its ascent with the hydrothermal system to trigger a magmatic-hydrothermal eruption. The fine ash fraction, which is generally scarce in all BdC deposits, is also richer in S, Cu, Zn, Pb, and As than the juvenile components of other La Fossa cone units, suggesting that the BdC eruption involved an interaction with a hydrothermal system anomalously enriched in S and metals (Fulignati et al. 1998).

Activity at La Fossa before the Breccia di Commenda eruption

The large amount of lithics which characterizes the BdC eruption can be related to the material

182 emplaced during previous eruptive events. We thus briefly summarize below pre-BdC activity at La
183 Fossa, based on available literature reconstructions (Fig. 2a). A re-examination of the volcanic
184 evolution of the La Fossa cone between the 12th and 13th centuries AD (which involved emplacement
185 of the Palizzi eruptive unit) was presented by Di Traglia et al. (2013). According to Di Traglia et al.
186 (2013), the Palizzi Eruptive Unit was fed by summit vents and consisted of four explosive phases
187 (PAL A to PAL D) and two effusive phases (that emplaced the Commenda rhyolitic lava and the
188 Palizzi-Campo Sportivo-Punte Nere trachytic lavas). The entire cycle resulted in a significant growth
189 in size and elevation of the cone itself (Di Traglia et al. 2013).
190 In the reconstructions of Keller (1980) and Di Traglia et al. (2013), the trachytic effusive phases of
191 the Palizzi eruption consisted of the emission of the Punte Nere delta (east), the Campo Sportivo
192 (north) and the Palizzi (south) lavas. On the other hand, De Astis et al. (2013), suggested based on
193 previous datings that the Punte Nere lava were much older (4.6±1.7 ka, Frazzetta et al. 1984;
194 5.3±2.2/1.1 ka to 3.8±0.9/0.8 ka, Soligo et al. 2000) than the Palizzi-Campo Sportivo trachytic lavas
195 (1.6±1.0 ka, Frazzetta et al. 1984; 1.5±0.2 ka; Voltaggio et al. 1995). According to this scheme, the
196 outpouring of the rhyolitic Commenda lava occurred between the Punte Nere and Palizzi events
197 (2.2±1.3 ka, Frazzetta et al. 1984; 2.1±0.3 ka, Voltaggio et al. 1995; De Astis et al. 2013), whereas it
198 post-dates the Palizzi-Campo Sportivo-Punte Nere lavas according to Di Traglia et al. (2013). Its
199 stratigraphic position still remains debatable, but all reconstructions agree that the Commenda lava is
200 older than the BdC eruptive sequence.
201 The stratigraphic position of BdC deposits, in turn, is consistently on top of both the Palizzi and
202 Campo Sportivo lavas (Supplementary Material). Although dating efforts are not in complete
203 agreement (cf. Frazzetta et al. 1984; Soligo et al. 2000; Arrighi et al. 2006), the Punte Nere lava shares
204 the same stratigraphic position (immediately below the BdC deposits) as, and have identical chemical
205 compositions, the Palizzi and Campo Sportivo lavas, suggesting that it could have been emplaced in
206 the same period (Supplementary Material). Whatever the case, at least two important lava effusions
207 (Campo Sportivo and Palizzi) took place immediately before the BdC eruption, with the possible

addition of the Punte Nere and Commenda lavas.

Methods

Stratigraphic logs and field observations were carried out at ~150 natural outcrops and at ~20 machine-excavated trenches at increasing distances from the La Fossa cone, where the current topography is flat enough to allow a good accumulation of both primary and secondary deposits. All the stratigraphic information is reported in a Google Earth© .kmz file where the sections with thickness of the various layers are detailed (see Online Supplement).

Bulk samples (of ~2 kg each) for layers 2b and 2c were first dried and then mechanically sieved from -4ϕ to 5ϕ at 0.5ϕ intervals (where $\phi=-\log_2 d/d_0$, d being the particle diameter and d_0=1 mm) for grain size analysis. To gain information on the source of the lithic material contained in the BdC deposit, we investigated the nature and the relative abundance of the different rock protoliths. At each locality, 100 clasts with diameters in the range 5-10 cm were randomly hand-picked. This clast size represents, on average, a small volumetric fraction of the bulk deposits (Layers 2b and 2c) analysed for grain-size. To classify rock fragments according to their lithology and composition, each fragment was broken in the field and observed with the aid of a hand lens. Plots of the data were expressed as percentage of different protoliths.

The volumes of the initial tephra fall deposits (Layers 1a and 1b) were calculated following Pyle (1989) and Bonadonna and Costa (2012), and those of the PDC deposits were obtained by integrating the thickness variation of deposits. The PDC deposits derived from Phase 2 (Layers 2a and 2c) were sampled at 22 sites and processed for grain-size analysis. The new field and grain-size data were integrated with the dataset presented by Gurioli et al. (2012).

Both stratigraphic observations and field data were also used to infer the state of the summit area and shallow hydrothermal system before the eruption, its role in eruptive dynamics and as input parameters for physical modelling (see Appendix for model). The model applied in this paper aims at describing the paroxysmal stage of the eruption (Phase 2). Our modelling, given in Appendix A,

considers the explosion dynamics and ballistic-block ejection, as well as the emplacement of Layers 2a and 2b from turbulent, stratified PDCs.

The BdC deposits have inherent spatially non-uniform features and their structure (see "Stratigraphy, sedimentology and analysis of the erupted products") suggests emplacement under strongly unsteady conditions, making simplified models difficult to apply. Moreover, the wide spectrum of grain sizes hinders the use of dusty-gas models, which cannot describe thermal and mechanical non-equilibrium processes. We therefore applied a transient, three-dimensional non-equilibrium Eulerian-Eulerian multiphase flow model (Neri et al. 2003; Esposti Ongaro et al. 2012) which as able to simulate the dynamics of the explosion, and a coupled Lagrangian model (de' Michieli Vitturi et al. 2010) to describe the trajectories of ballistic blocks. While the Eulerian formulation is more suited for a large number of particles, strongly coupled with the gas phase (i.e., for particles with diameters below about 1 mm), a Lagrangian approach is more appropriate for loosely coupled regimes (i.e., particles above a few cm; Cerminara et al. 2015). We have verified that the two formulations are equivalent (both physically and numerically) for particles in the lapilli range (2 to 64 mm). To solve the model equations numerically, we have developed a new solver with OpenFOAM, an open-source computational infrastructure for Computational Fluid Dynamics. The coupled model and the new numerical code are presented in detail in the Appendix.

The model assumes that the explosive phase 2 was triggered by the sudden exposure to atmospheric pressure of the shallow hydrothermal fluids, initially at high pressure and temperature. This is a 3D equivalent to the "top-down" model for hydrothermal explosions by McKibbin et al. (2009), but the effect of the flashing of the superheated fluids and the subsequent downward migration of the boiling front are not taken into account here, as water is considered as already vaporized.

Stratigraphy, sedimentology and analysis of the erupted products

Our proposed stratigraphic reconstruction of the BdC event is similar to that proposed by Gurioli et al. (2012), from which we take the distinction of the three main phases (Phase 1, Phase 2, Phase 3)

260 which can further subdivided into different layers (Fig. 2b). Based on stratigraphic correlations (Fig.
261 3) and considering the thickness variation shown by the lowermost unit (emplaced during Phase 1,
262 and hence representing the opening phase of the eruption), we define two distinct layers (1a and 1b)
263 representing ash fallout deposits separated by the Rocche Rosse tephra and having different dispersal
264 areas (Fig. 4a). The lowermost layer (Layer 1a) has a westward dispersal, while Layer 1b has a
265 southward dispersal.
266 Deposits associated with Phase 2 can be divided into four layers (2a through 2d). In agreement with
267 the reconstruction of Gurioli et al. (2012), Layers related to Phase 2a are mostly dispersed in the
268 south-eastern, eastern and north-western sectors. However, our reconstruction indicates an extension
269 of the maximum distance attained by the ballistic blocks and the associated PDCs. Large ballistic
270 blocks (up to 30 cm in diameter), accompanied by high concentrations of ballistic blocks per area
271 (several blocks per square meter), were documented in the field up to about 2100 m from the crater
272 (s151, Fig. 1c). The high concentration of impact craters produced by block fallout in the south-
273 eastern sector of La Fossa cone resulted in a systematic disruption of the original ash fall succession
274 at the base of the BdC sequence (Fig. 5a, b, c). Layer 2a consists of an ash-poor, topography-draping
275 and filling, PDC deposit which was emplaced together with the ballistic block shower. This deposit
276 covers more than 4.7 km^2 with a minimum volume of 2.8×10^6 m^3. In proximal to medial sites, PDCs
277 and ballistic blocks are admixed together, suggesting that they were deposited almost simultaneously
278 (Fig. 5c). It is worth noting that the blast-like nature of the Layer 2a PDCs is confirmed by their
279 capability to easily overpass a topographic barrier as high as 175 m at a distance from the source of
280 about 2 km in the south-eastern direction. The thickness and coarse grain-size of Layer 2a in the distal
281 outcrop (s151, Fig. 1c) suggest that the dispersal of the PDC was greater than mapped here.
282 The Layer 2a PDC was immediately followed by a PDC which emplaced an ash-rich, thinly-stratified,
283 dune-bedded deposit (Layer 2b), with a thickness varying between 0.1 and 0.3 m but significantly
284 less dispersed as compared to Layer 2a (Figs. 4c, 5d). The different areal distribution of Layer 2a
285 (with a longer run out towards east and west) with respect to Layer 2b (south-directed) suggests that

286 the two layers might have originated from wo different pulses in the eruption sequence that made up
287 Layer 2 (Fig. 4).
288 Phase 2c consisted of the emission of dense PDCs which led to the emplacement of massive deposits
289 ranging from 0.8 to 3.5 m in thickness (Layer 2c; Fig. 5d, e), mostly concentrated on the lowermost
290 flanks and at the foot of La Fossa cone. They cover a total surface of 0.44 km^2 with a volume of 1.39
291 $\times 10^6$ m^3. The distribution of Layer 2c is neither regular nor ubiquitous around the cone (Fig. 4d),
292 likely reflecting the vent location and the control played by the uneven height of the crater rim (i.e.
293 the likely represent boiling-over activity, where directions of over-flowing PDCs are controlled by
294 the geometry of the crater rim). The coarsest breccia deposit (with boulders up to 1.5 m in diameter)
295 was observed along the shoreline between Punte Nere and Porto di Levante bay (Fig. 6a), suggesting
296 that the BdC source vent was located close to the northernmost sector of the La Fossa crater area and
297 that a part of the deposit likely entered the sea. In this area, and in the Palizzi valley, vertical, fines-
298 poor pipe structures are abundant and well preserved in the deposit (s23 in Fig. 1c). Massive, boulder-
299 rich (less than 1 m in diameter) breccia deposits are also present in the Palizzi valley at the break-in-
300 slope at the foot of the La Fossa cone (Fig. 6b). On the south-eastern flank of La Fossa, Layer 2c is
301 overlain by an ash-rich, accretionary lapilli-bearing deposit (Layer 2d) which possibly represent co-
302 PDC deposits emplaced immediately after the breccia (Fig. 5f).
303 Phase 3 comprises grey to red ash fall deposits separated by at least three layers related to Rocche
304 Rosse tephra. As described by Gurioli et al. (2012), these deposits have been observed dominantly in
305 the southern and eastern sectors of La Fossa, suggesting dispersal toward the southeast. The lower
306 part of Phase 3 (Layer 3a) is represented by a series of lithic-rich, “wet” layers of vesicular tuff bearing
307 non-structured accretionary pellets, which represent, waning, ash-emission, tail of the eruption
308 (Gurioli et al. 2012). In the Palizzi valley and on the northern side of the La Fossa cone, the Rocche
309 Rosse tephra layers are observed interbedded with a 1-m thick, massive, matrix-supported ash and
310 pebble deposits (lahar units; Layer 3b). These stratigraphic features suggest that deposition and
311 reworking of the primary ash fall occurred close in time.

Nature of lithic material in the BdC deposits

The deposits related to the BdC eruption are characterized by a large amount of lithic material, mostly consisting of angular lava fragments (Fig. 6). Understanding the origin of this lithic material is thus crucial in understanding the structure of the summit area when the BdC vent opened, with a secondary aim being to locate the position of the vent during the eruption. To do this, we integrated the componentry analysis of the matrix (coarse ash) carried out by Gurioli et al. (2012) with a systematic observation of protoliths at key locations. The sampling sites, as well as the results of the classification and relative abundances of different rock types, are reported in Fig. 7. Results highlight that, at different sites, the relative abundances of different protoliths are comparable where the large majority of the examined rocks (56-70%) consists of lavas, ranging from fresh to poorly altered, and from dense to vesicular (Fig. 6e). All fresh and poorly altered lava clasts bear mm-sized crystals of feldspar and pyroxene set in a fine-grained groundmass consistent with an intermediate composition (trachyte). This category is followed in abundance (15-20%) by moderately to strongly altered lavas. The moderately altered lavas are also intermediate in composition (trachytic), the deeply altered lavas being difficult to classify. Hydrothermally altered tuffs were identified as the third most abundant category (15-24%).

Clasts of welded scoria were found only in the site north of La Fossa cone (15%), and flow banded rhyolitic lavas and fresh, trachytic lava clinkers were only sporadically present in the deposits located in the southern sites (Fig. 7). Because these less abundant rock types only occur at specific locations and each type is present only in outcrops located downslope of sites where the same rock crops out, we interpret their presence as due to incorporation of this material during flowage of the PDCs from the crater area towards the valleys (i.e., their presence results from a bulking processes). In support of this hypothesis, flow banded rhyolitic lavas are only present downslope of the rhyolitic Commenda lava, welded scoria downslope of the Punte Nere area, and fresh trachytic lava clinkers downslope of the Palizzi lava flow.

Our analysis of the breccia protoliths, as well as that of Gurioli et al. (2012), suggest that: (i) during the course of the BdC eruptive activity, a large volume of old material, especially lavas of shallow origin altered by fumarolic activity, was ejected; (ii) the dominant part of these products consisted of lava clasts of trachytic composition, from fresh to moderately altered, with texture and composition similar to the trachytic lavas issued at the end of the Palizzi eruptive unit; (iii) only a limited amount of the rock fragments in the breccia is constituted by clasts derived from material outcropping upstream of each sampling site; (iv) the possible juvenile origin of a part of the fresh lava clasts seems unlikely as no evidence of rapid quenching (glass rinds or radial jointing) was detected in the analysed clasts. Moreover, no blocks or bombs show evidence of heating of the surrounding finer matrix, as commonly seen in halos formed upon contacts of ash with bombs at nearly magmatic temperatures.

Grain-size analysis

In addition to the data derived from the 22 sites sampled in this work (Fig. S6 in the Supplementary Material), data from Gurioli et al. (2012) were used to depict the overall grain-size characteristics of PDC deposits related to Phases 2a and 2c (Figs. 8, 9). Grain-size data of Layers 2a and 2c form two discrete groups on both the Mdϕ (median)-σϕ (sorting) and F1 (% fraction ≤1 mm)-F2 (% fraction ≤1/16 mm) diagrams (Fig. 8). Mdϕ of Layer 2a varies from -5.1 to 2.1ϕ, whereas σϕ varies from 1.2 to 3.4. F1 accounts between 90.9 and 5.5% and F2 represents from 0 to 9.8% of the total. In contrast, Layer 2c is distinctive because of its lower sorting, irrespective of absolute grain-size. The deposit also shows the largest range in Mdϕ (from -5.8 to 3.2ϕ), σϕ (1.4 to 3.7), F1 (17.0 to 95.6%), and F2 (0.2 to 33.0%). Layer 2a is thus generally better-sorted with respect to Layer 2c, with an evident lack in fine (<0.063 mm) material, and having a unimodal distribution (Fig. 8). On a plot of F1 vs F2, samples of Layer 2a occupy the area below the field of PDCs (Fig. 8b), indicating either a reduced fragmentation at the source vent or a significant depletion of fines during transport, or both. The grain-size distribution of Layer 2a is similar to that of high energy blasts deposits (i.e. Layer B, defined as s "strongly depleted by fines and thus has a clast-supported fabric with open voids between

364 clasts" in Belousov et al. 2007), such as the 1902 Mt. Pelee (Martinique; Lajoie et al. 1989), 1957
365 Benzymianny blast (Russia; Belousov 1996), the 1980 Mount St. Helens blast (USA; Hoblitt et al.
366 1981), and the Boxing Day, 1997 Soufriere Hills blast (Montserrat; Ritchie et al. 2002). In particular,
367 it shows close similarities with the hydrothermal blast deposit produced during the 2012 Te Maari
368 eruption at Mt. Tongariro (New Zealand; Lube et al. 2014).
369 Compared with typical pumice-rich, high-concentration PDC deposits (Fig. 8a), Layer 2c is relatively
370 ash-poor and relatively well-sorted, likely reflecting the weaker fragmentation of lithic material
371 compared to fragile highly vesicular pumice both at the source vent and during transport.
372 Fragmentation during transport of PDC 2c had a limited role as all PDCs travelled less than 1300 m
373 from the summit of the La Fossa cone.
374
375 **Modelling the explosion dynamics of the *BdC* eruption**
376 Based on the observation that a phase of effusive activity shortly preceded the BdC eruption, and on
377 the character of the lithic material which largely comprises the breccia deposit, we assumed that the
378 exploding volume was initially confined within the La Fossa cone crater area, which was possibly
379 filled by lava from the previous effusive eruptions. Magma degassing through the volcaniclastic
380 material from previous eruptions and the overburden of the crater-filling lavas provided the necessary
381 conditions for the build-up of the interstitial gas overpressure. This scenario is compatible with
382 continuous degassing, including fumarolic. When this fluid overpressure exceeded the tensile strength
383 of the overlying lava cap, a breakdown occurred (not modelled here), exposing the porous material
384 and hydrothermal system fluids to atmospheric pressure. The explosion was then driven by the rapid
385 decompression of the fluids and the fragmentation of the porous material into a gas-particle mixture,
386 made up of water vapour, ash and lithic blocks. This was subsequently accelerated during expansion
387 in the atmosphere. In this stage, the blocks were ejected ballistically from the vent, while the ash
388 fraction was mechanically coupled with the eruptive plume. Lateral expansion and the rapid collapse
389 of the gas-particle jet generated turbulent PDCs. The numerical model used in this work aims at

390 simulating the event starting from the decompression and acceleration of the mixture of
391 overpressurized fluids and the already fragmented material, described by a Eulerian ash+lapilli
392 fraction and a Lagrangian block-particle fraction (Neri et al. 2003, Esposti Ongaro et al. 2012; de'
393 Michieli Vitturi et al. 2010).
394 Recent field/experimental studies have addressed some of the parameters controlling the dynamics
395 and energetics of explosions due to decompression of a hydrothermal system, including the type of
396 rock involved in the eruptive event and its porosity, permeability and strength, as well as the type and
397 amount of fluid involved in the explosion and initial pressure-temperature (P-T) conditions. For the
398 Te Maari case, experimental works have thus been conducted in a range of temperatures (200 –
399 350°C), pressures (4 – 6.5 MPa) and lithology (Montanaro et al. 2016).
400 We apply a parametric approach, focusing on the three parameters that mostly control the dynamics
401 of the explosion of a pressurized shallow body of mass (M): the initial pressure (P_0), gas content (n)
402 and temperature (T). The total erupted mass in phases 2a+2b ranges (Table 2) from 7.5×10^8 kg (3×10^5
403 m^3 Dense Rock Equivalent, DRE) to 2.5×10^9 kg (10^6 m^3 DRE), with the lower bound being
404 constrained by the measured volume of the pyroclastic deposit, and the maximum value estimated by
405 considering mass not deposited or eroded.
406 The initial gas mass fraction (n) is related to the porosity of the exploding material (ϕ) by:

407 $$n = \frac{\phi\rho_g}{(1-\phi)\rho_s + \phi\rho_g}$$

408 where ρ_g is the density of the gas phase, and ρ_s is the density of the solid phase, with $\rho_g = \frac{P}{RT}$, with
409 P, R and T being pressure, the specific gas constant and temperature, respectively. We vary the
410 porosity of the exploding body in a realistic range, from 0.3 to 0.7 (this is intended as a cell-averaged
411 value for the hosting system, not the porosity of individual clasts). Based on experimental works by
412 Montanaro et al. (2016), overpressure is varied from 6.0 to 20.0 MPa. Mixture temperatures of either
413 523K or 623K have been considered (250-350°C).
414 The available specific energy (per unit of mass) for an adiabatic (but almost isothermal) explosion

415 depends on the amount of compressed interstitial gas and can be estimated as (Wilson 1980):

416 $$\mathrm{E}_{iso} = nRTln\left(\frac{P_0}{P_{atm}}\right) \cong \frac{1}{2}U^2$$

417 where R is the gas constant, n is the mass fraction of gas, P_0 is the pressure at the vent, P_{atm} is the
418 atmospheric pressure, and U is an estimate of the ejection velocity. For the reference case (Run F-
419 N35E in Table 3), $\mathrm{E}_{iso} \cong 54 \times 10^3$ J/kg, corresponding to an (over)estimated ejection velocity of
420 about 320 m/s. In fact, in our simulations, ballistic blocks never reach such a velocity, due to the
421 rapidity of the gas decompression and the delay in particle coupling.
422 The Digital Elevation Model with a spatial resolution of 1 m of the present island of Vulcano is used,
423 but with the crater filled to the rim by pre-BdC lavas and a shallow, elongated fissure excavated within
424 it. Such a geometry was chosen because we observed that it favours the generation of asymmetric
425 PDCs and ejection of ballistic blocks in the direction orthogonal to the fissure main axis, as observed
426 in the field. The width and depth of the fissure is set to fit the measured total mass (or DRE volume)
427 of the eruptive products. The fissure is filled with a compressed gas-particle mixture, thus assuming
428 that the eruptive mixture immediately fragmented during decompression (as in Clarke et al. 2002).
429 Because the energy of fragmentation (1.8 - 4.8 MPa; Spieler et al. 2004; Mayer et al. 2016; Montanaro
430 et al. 2016) in the envisaged porosity range is lower than the assumed overpressure (12 MPa), this is
431 equivalent to a maximum underestimation of 40% of the initial pressure needed to trigger the
432 explosion (see also Esposti Ongaro et al. 2012). In addition, altered rocks can have lower
433 fragmentation thresholds (up to 50% lower; Mayer et al. 2016; Montanaro et al. 2016c).
434 Finally, the Eulerian-Eulerian eruptive mixture in our model is represented by one gas phase and one
435 particle phase of 2 mm diameter. The Eulerian particle phase should be considered as a hydraulically
436 equivalent particle class representing pyroclasts in the ash-lapilli range (simulations with particles of
437 1 mm or 4 mm do not show significantly different explosion dynamics, Esposti Ongaro et al. 2012).
438 Three ballistic-block classes of 8, 16 and 30 cm diameter (based on our field measurements) were
439 used as Lagrangian phases.

Numerical simulation results

Fig. 9 and Supplementary movie 1 depict the temporal and spatial evolution of the eruptive mixture made of gas, ash particles (2 mm) and blocks (8-30 cm) obtained from the numerical model. During the first 3-4 seconds (Fig. 9), the mixture expands almost isotropically, due to the dominant effect of the high-pressure gradient. This is the stage of rapid decompression (the *burst* phase of Esposti Ongaro et al. 2012) which is able to accelerate the mixture up to vertical velocities slightly exceeding 200 m/s. These are higher than those measured in analogous laboratory experiments (around 160 m/s; Montanaro et al., 2016c) probably due to the lack of the material yield strength and higher initial pressure. Blocks accelerate to comparable velocities of gas and lapilli due to drag forces and pressure gradient. Lateral surge velocity is, during this stage, of the same order of magnitude, and asymmetry/anisotropy of the fissure can direct ballistic blocks in preferential directions. In this case, ballistic blocks located initially in the centre and along the eastern margin of the fissure are preferentially driven towards the ESE.

After the burst stage (from 5 s to about 15 s, Fig. 9), compressibility effects (shock waves) create a vent-ward atmospheric motion that arrests the lateral surge motion and pulls the plume upward. In this stage, the fissure shape plays an essential role, as the "suction" effect occurs only along the direction of the fissure. Orthogonal to the fissure, the mixture collapses under the effect of gravity, forming PDCs. At the same time, ballistic blocks have reached their maximum altitude and decouple from the gas-particle mixture (typically particles >8 cm in our simulations), spreading radially under the dominant effects of inertia and atmospheric drag forces. After reaching a maximum height of about 1500 m above sea level, the whole eruptive plume collapses, generating a second, major PDC, preferentially directed orthogonal to the fissure direction. At 40 s after the beginning of the event (Fig. 9), almost all ballistic blocks have landed, while PDCs are still propagating. The maximum distance reached by ballistic blocks of up to 30 cm diameter, ejected towards the East, is comparable with that observed in the field (2 km). The maximum flow run-out (>3 km orthogonal to the eruptive

466 fissure and 1.5 km along the fissure direction) is then reached after about 60 s.

467 Numerical simulations demonstrate that the observed PDC deposits and ballistic-block ranges are
468 consistent with an erupting mechanism driven by the explosion of a shallow (non-magmatic)
469 pressurized body. Different initial fissure geometries were tested in this work, both circular and
470 elongated, and with different aspect ratios. Circular vents produce axisymmetric ejection, while
471 explosions that were too shallow (less than 100 m) were too short-lived to accelerate ballistic
472 fragments sufficiently to fit the observed ranges. Our best match is thus obtained with explosions
473 from an elongated, asymmetric body measuring about 200 m in length and 80-100 m in width, located
474 northeast of the present crater. With the imposed volumetric constraint, this results in a 150-180 m
475 fissure depth. Although errors are very difficult to estimate systematically, the parametric study
476 suggests a mass of $1.5\pm0.5\times10^9$ kg, an initial overpressure of 12±3 MPa, a maximum temperature of
477 250±50°C and an initial porosity between 0.3 and 0.6. It is worth remarking that simulations with
478 higher temperature of the exploding mixture tend to be more convective, hindering the formation of
479 intense PDCs. This observation supports the idea that the involvement of significant amount of fresh
480 magma is unlikely in this stage since it would have significantly raised the initial temperature of the
481 system.

482

483 **Discussion**

484 *Dynamics of the BdC eruption*

485 The BdC eruption started with two distinct lithic-rich ash emissions (Phases 1a and 1b). The onset of
486 the eruption at La Fossa was pene-contemporaneous with explosive activity at the Rocche Rosse vent
487 on Lipari Island (Fig. 10). The eruption suddenly escalated to its paroxysmal stage (Phases 2a and
488 2b) consisting of the ejection of ballistic blocks mainly directed SE and in the flow of unsteady,
489 stratified PDCs across the entire central sector of the La Fossa caldera. Layer 2a consists of an ash-
490 poor, topography-draping, blast-like deposit which was emplaced together with the ballistic block
491 shower. The blast was immediately followed by surge-like PDCs which emplaced ash-rich, thinly-

492 stratified, dune-bedded deposits (Layer 2b). Gurioli et al. (2012) reported PDC deposits of Layer 2a
493 only confined to the southern and eastern sectors. The 17 new stratigraphic trenches that we dug
494 around La Fossa cone, allows us to extend this limit beyond the La Fossa caldera walls, highlighting
495 also a north-western and south-eastern dispersal. Dense, gravity-controlled PDCs (Layer 2c) were
496 next generated. These were immediately followed by the accumulation of co-PDC, accretionary
497 lapilli-bearing, ash deposits (Layer 2d). The descent of the dense PDCs of Layer 2c occurred only
498 through the lower parts of the crater rim, suggesting that the PDC generation mechanism was by
499 boiling-over activity. Regularly-spaced, vertical, fines-poor pipe structures are abundant in the Palizzi
500 valley and in the outcrops of Layer 2c situated in the easternmost part of the Porto di Levante bay
501 (Fig. 6c). Degassing structures are suggestive of a sudden deflation of fluidized PDC masses as they
502 came to rest at the foot of the cone, possibly combined with a phenomenon of gas release from porous
503 lithic clasts following the sharp decompression due to explosion. The observation reported by Gurioli
504 et al. (2012), of vertical pipe-like structures originating from large, lithic, hydrothermally altered
505 blocks of Layer 2a, and crossing the deposit of Layer 2b, suggests that the emplacement of Layers 2a
506 and 2b occurred close in time, as fluids were still being vigorously released from porous lithic clasts
507 of Layer 2a by the time the ash-rich Layer 2b was deposited. On the other hand, the burial of the same
508 degassing structures by Layer 2c is indicative of a longer time interval between the emplacement of
509 Layers 2b and 2c. We hypothesize that the increase amount of fine (<0.063 mm) material, from Layers
510 2a to 2c, is related to the different rock lithologies within the crater. Initially the ejection of the lavas
511 topping the source area produced coarse-grained, fines-poor deposits (Layer 2a), later the eruption
512 disrupted the underlying poorly consolidated and altered tuff deposits, generating a higher amount of
513 fine material (Layers 2b and 2c).
514 In the final phase, BdC fallout deposits are interfingered with at least three Rocche Rosse tephra beds
515 from Lipari. This clearly testifies that explosive activity in Lipari and Vulcano went on for some time
516 contemporaneously. The ash deposit rich in accretionary lapilli (Layer 2d) was likely due to
517 secondary explosions produced by the vapour generated by the entrance of PDCs into the sea, as

518 already observed at Soufriere Hills volcano, Montserrat (e.g., Mayberry et al. 2002; Carn et al. 2004;
519 Burns et al. 2017). In contrast, the presence of non-structured ash pellets within the vesiculated tuffs
520 of Phase 3, coeval with reworking processes, suggests that wet environmental conditions affect ed
521 both the eruptive plume and the emplaced ash deposits, eventually triggering lahars in the north-
522 eastern sector and creating small mud ponds in the Palizzi valley.
523 Some controversial hypotheses exist in the literature regarding the presence of juvenile material in
524 the BdC deposits. In fact, while Frazzetta et al. (1983), De Astis et al. (2006, 2013) and Dellino et al.
525 (2011) propose that no juvenile fraction can be clearly identified, Gurioli et al. (2012) suggest that
526 fresh glass material showing a large chemical variability from rhyolitic to trachyandesite does occur
527 mostly in the finer fraction of the deposits (ash and lapilli) as well as in some bombs. This material,
528 which is commonly below 40 vol.% of the deposits, frequently has fine ash adhering to grain surfaces
529 and filling vesicles, with glass shards characterized by altered patinae. We did not identify a clear
530 juvenile fraction in the coarsest clasts of the deposit, which also show no evidence of rapid quenching
531 or interactions at high temperatures with the embedding, cooler finer matrix. Although definitive
532 proof for either demonstrating or excluding the involvement of fresh magma in an eruption is not
533 always straightforward, it has been recently pointed out that the presence of wide ranges of glass
534 compositions (partially overlapping those of vent-area country rock), microlite textures and mineral
535 content variability in glassy particles of deposits related to events with a strong hydrothermal
536 signature, is difficult to reconcile with involvement of fresh magma (Pardo et al. 2014). In fact, while
537 several eruptions at La Fossa are heterogeneous because of mingling and mixing processes of small
538 magma batches (Gioncada et al. 2003), these commonly show a predominant composition with minor
539 contributions recorded as enclaves, while in the BdC event the chemical variability appears to be
540 equal in volume, at least for the trachytic to rhyolitic end-members (Gurioli et al. 2012). If the eruptive
541 mixture included a minor juvenile fraction of variable composition of sufficient volume to flash the
542 hydrothermal system, this was small and cannot be unequivocally identified in the emplaced deposits.
543

544 *Pre-eruptive state of the crater area and location of the BdC vent*

545 Stratigraphic observations coupled with the recent reconstructions of the Palizzi eruptive period (Di
546 Traglia et al. 2011; De Astis et al. 2013), clearly show that the final eruptive period immediately
547 before the BdC eruption consisted in a phase of effusive activity. The tight time relationship among
548 the lava effusions and the BdC event is further constrained by the absence of lithic lava clasts in the
549 previous PAL D fallout deposit, and by the lack of significant primary deposits between the lavas and
550 the BdC tephra sequence (Supplementary Material). The state of moderate alteration of the lava
551 fragments in the BdC deposits (fresh and moderately altered fragments account for more than 60%
552 of the studied blocks) is also in agreement with a short time lapse of exposure to fumarolic action
553 (about a century and a half) between the emplacement of lavas and their ejection as lithic material
554 within the BdC deposits. The roots of the Palizzi and Commenda lavas can be nowadays clearly seen
555 in the inner part of the present crater rim to be immediately below the BdC sequence. Moreover,
556 geophysical surveys also revealed the presence of a buried lava body in the south-eastern part of the
557 La Fossa cone (Fig. 7; Blanco-Montenegro et al. 2007; Barde-Cabusson et al. 2009; Napoli and
558 Currenti 2016). In particular, Barde-Cabusson et al. (2009) suggested that the minimum depth of the
559 geophysical anomaly can be estimated to ~50 m, in the range of the tephra pile emplaced after the
560 Palizzi eruptive Unit (Commenda Eruptive Unit and Gran Cratere Eruptive Cluster; Di Traglia et al.
561 2013). All this evidence supports the idea that the final effusive activity immediately before the BdC
562 event clogged the crater area with lava. This hypothesis is also supported by comparison of the
563 volume of the lava material forming Layer 2a (2.8×10^6 m^3 by considering the whole deposit as
564 entirely made by lava lithics) with that of a hypothetical lava cap having a diameter comparable with
565 the present crater geometry (600 m) and an average thickness of 10 m.

566 The presence at the end of the Palizzi eruption of lava in the summit part of the cone, which eventually
567 flattened the summit area, can also explain the decrease of gas permeability and build-up of the
568 overpressure necessary to overcome the tensile strength of rocks in the initial part of the explosion.
569 The estimated overpressure from numerical modelling (12±3 MPa) is consistent with values

570 associated with the combined effects of the increased lithostatic load due to the lavas filling the crater
571 (P_L~3.5 MPa assuming a depth of the lava filling the crater H=200 m and a density of 1750 kg/m^3)
572 plus the pressure associated with magmatic gas flux through the porous matrix (P_G ~10 Mpa for a
573 permeability of degassed lavas of 10^{-12}, accordingly to Woods et al. 2002).
574 Regarding the location of the BdC vent, we suggest a possible location in the north-eastern sector of
575 the La Fossa cone. This hypothesis is supported by the presence of the largest boulders (more than
576 1 m in diameter) observed in the northern outcrop near the coast (Fig. 6a). Moreover, the agreement
577 between field data and numerical simulations of Phase 2a is more consistent with this location of the
578 fissure vent.
579
580 *Limitations and constraints of current modelling approach*
581 Concerning the above model-derived pressure estimates, two additional factors should be considered.
582 On one hand, depending on the amount and temperature of the available liquid water, the energy for
583 fragmenting and sustaining the explosive phase might be much higher if steam-flashing was
584 considered. This in turn would affect the efficiency in producing fine material which could feed both
585 PDCs and ash plumes (Mayer et al. 2016; Montanaro et al. 2016a,c). In such a case, it is likely that
586 the overpressure required to produce the observed phenomenology would be significantly lower. On
587 the other hand, if the effect of the cohesive stress was taken into account (McKibbin et al. 2009) the
588 required initial overpressure would increase. The balance between these two factors is difficult to
589 estimate. However, accurate measurements of rock porosity/permeability, together with constraint of
590 rheological properties will likely help to add further constraints to the estimated initial pressure.
591
592 *Comparison with other phreatic/hydrothermal eruptions*
593 The blast phase of the BdC eruption (Phase 2a) shows strong similarities with recent events directly
594 observed at Soufrière-Guadeloupe (14 September 1976 blast; Sheridan 1980; Hincks et al. 2014), Te
595 Maari-Tongariro (6 August 2012; Lube et al. 2014) and Ontake (27 September 2014; Maeno et al.

596 2016). Deposit characteristics of the BdC blast also resemble that of other historic events such as Zao
597 1895 (Fujinawa et al. 2008; Miura et al. 2012), Bandai 1888 (Yamamoto et al. 1999; Fujinawa et al.
598 2008), and Adatara 1900 (Fujinawa et al. 2008). Hydrothermal/phreatic blasts can occur as isolated
599 events with little or no precursors (as at Bandai, Te Maari-Tongariro, Ontake) or within a phase of
600 volcanic unrest (as at Zao, Adatara, and Soufrière-Guadeloupe). The BdC eruption apparently belongs
601 to the second category, showing an initial weak ash emission (Phases 1a and 1b) preceding Phase 2a
602 (the blast phase).
603 The features of the blast phase are also similar to those described for other hydrothermal eruptions,
604 in terms of the lithic-rich nature of the components, volume of the products (between 10^{-6} and 10^{-3}
605 km^3), short duration of the events, and strong directionality of the explosions, especially for the
606 ballistic blocks and dilute PDCs (Table 4). Simulated PDCs propagate as turbulent, stratified currents,
607 with maximum ash volume concentration of about 0.005. Their maximum temperature is higher
608 (exceeding 200°C) than that observed at Ontake (where temperatures within the PDCs were mostly
609 below 100°C), probably due to the more dilute conditions (Maeno et al. 2016), but they are consistent
610 with those measured at Te Maari (about 280°C; Lube et al. 2014), indicating that the initial
611 temperature of the hydrothermal body is conserved during the blast phase (Esposti Ongaro et al.
612 2012). This is also similar to the average fumarole temperature currently measured at La Fossa, which
613 is further support for our hypothesis. While there is little sedimentological evidence of PDCs
614 associated to phreatic and hydrothermal events (because their small volume and thickness hinder their
615 preservation), high-energy, dilute and low-temperature PDCs associated with explosion of a
616 hydrothermal system should be more common than previously postulated.
617 The vents of the Soufrière-Guadeloupe, Te Maari-Tongariro, and Ontake eruptions were also
618 described as elongated fractures (consistent with our findings from the numerical modelling)
619 accounting for the directionality of the PDCs (Sheridan et al. 1980; Lube et al. 2014; Oikawa et al.
620 2016). However, in nature, further complexity can be observed in both the spatial and temporal
621 evolution of a vent system; this was not possible to address in numerical simulations. For example,

622 inclination of the fracture opening would likely enhance directional effects and fallout of ballistic
623 blocks in specific sectors around the volcano. At Te Maari, the westward directed blast was produced
624 by a series of explosions with a fragmentation front that migrated from west to east. As the lava was
625 fragmented, producing a large number of ballistic blocks, the fragmentation front migrated eastward
626 and different lithologies were involved; the ejection direction also changed, producing a different
627 distribution of the ballistics with time (Breard et al. 2014; Fitzgerald et al. 2014; Montanaro et al.
628 2016a).
629 Regarding the explosive mechanism, the Bandai and Te Maari-Tongariro events were triggered and
630 laterally directed by a combination of sudden depressurization of the hydrothermal system due to a
631 landslide, and lateral and localized vent opening (Yamamoto et al. 1999; Breard et al. 2014, 2015).
632 Additional complexity was observed at Te Maari, where potential fluid injection occurred weeks prior
633 to the eruption (Jolly et al. 2014) and the first blast actually was eastern-directed (in the opposite
634 direction to the landslide), while the second and most powerful blast was directed westward. For the
635 Zao and Soufrière-Guadeloupe eruptions (Fujinawa et al. 2008) an injection of magma at depth was
636 invoked as a triggering mechanism. The Ontake eruption seems to have been triggered by a
637 pressurized reservoir, potentially associated with the arrival of new magma, temperature increase, or
638 sudden critical phase change in the hydrothermal system (Kato et al. 2016; Maeno et al. 2016). This
639 latter case possibly best describes the triggering mechanisms that can be invoked for the BdC
640 eruption. In fact, the lack of evidence of a landslide, coupled with the reconstruction of the summit
641 area prior to eruption, suggests that the lavas filling the crater area possibly exacerbated a process of
642 pressure build-up within the hydrothermal system.
643
644 *Simultaneity of the BdC with the Rocche Rosse eruption from Lipari*
645 The simultaneity of the BdC and the Rocche Rosse eruptions suggests that links between the two
646 magmatic systems may exist. The last eruption on the Island of Lipari is thought to have been
647 triggered by the injection of mafic magma into a zoned latitic-rhyolitic magma chamber (Davì et al.

2009b). The absence of a hydrothermal system in the NE part of the Island of Lipari probably favoured the development of a pure magmatic eruption (Davì et al. 2011) with a large dispersal area (Bescoby et al. 2008; Albert et al. 2012; Caron et al. 2012), whereas the presence of a hydrothermal system within the La Fossa cone (Fulignati et al. 1998) favoured the high-energy hydrothermal pulsating eruption of Vulcano. In addition, there is evidence that a strong contribution to the development of a hydrothermal system occurred just towards the end of the Palizzi eruptive unit (Fulignati et al. 2018). Recent observations by Biggs et al. (2016) showed that volcanoes fed by magma bodies that are spaced less than about 10 km apart generally could have simultaneous eruptions, while stress changes can couple large eruptions over distances of about 20–40 km. Simultaneous activation of multiple vents can be particularly relevant in caldera settings (Roggensack et al. 1996; Pistolesi et al. 2016). In the case of the BdC and the Rocche Rosse eruptions (vents located 12 km apart) the magmatic and tectonic links have already been proposed by several authors (Ventura et al. 1999; Gioncada et al. 2003; Ruch et al. 2016), and concurrent eruptions could be facilitated by the occurrence of a stress change (large earthquake) along the Aeolian-Tindari-Letojanni fault zone. A similar coupled-event has been recognized at Tarawera volcano and at the nearby Waiotapu geothermal field (New Zealand). This has been attributed to a basaltic intrusion at depth, capable of triggering both a magmatic (the Tarawera rhyolitic) and the hydrothermal (Waiotapu) ~AD 1315 eruptions from vents situated more than 10 km one from the other (Nairn et al. 2005).

Possible occurrence of a new BdC-like eruption at Vulcano and associated hazards

The data presented here and the comparison with similar eruptions provide important insights into potential future hydrothermal eruptions at the La Fossa cone. The increase and decrease in pressure in the La Fossa cone hydrothermal system are responsible for maintaining high fluid permeability while maintaining existing fractures in the cone (Paonita et al. 2013; Capasso et al. 2014). Therefore, nowadays the low permeability conditions that would have affected the explosion during the BdC eruption are unlikely. However, it cannot be ruled out that the occurrence of landslides during periods

674 of high pressure can trigger a hydrothermal eruption like the Bandai and Te Maari-Tongariro events.
675 In addition, it should be considered that La Fossa cone pressurization may be one of the causes of
676 flank instability (Reid 2004; Thomas et al. 2004). Considering this, even in the absence of the same
677 predisposing factors of the BdC eruption (low permeability in the summit area), the increase in the
678 amount of gas in the hydrothermal system could promote internal volcano pressurization that might
679 in turn produce the increase in pore pressure and the consequent flank instability, generating
680 landslide-triggered hydrothermal explosions. In the same way, the possibility that a hydrothermal
681 eruption at La Fossa cone can be triggered by a strong release of gas from the magma chamber
682 following movements of the regional faults that are present in the Vulcano-Lipari area cannot be
683 excluded (Montalto 1995).
684 If a BdC-like eruption were to happen again at La Fossa, the impact on the island would be
685 catastrophic and far larger than that associated with a Vulcanian-type eruption. In fact, hazards
686 associated with a BdC-like eruption include both dilute and dense PDCs with a possible blast
687 component, intense and long-lasting tephra fallout and highly-concentrated sedimentation of ballistic
688 blocks up to 2 km from vent. Modelling of PDCs has in particular indicated a run-out up to 2.3 km in
689 the direction of Piano and more than 3 km towards the NW. Considering the proximity of residential
690 buildings and both critical facilities and infrastructures to La Fossa edifice and the high-to-very-high
691 vulnerability of the associated urban fabrics (Galderisi et al. 2013; Biass et al. 2016a,b), depending
692 on the position and the geometry of the eruptive vent, the resulting impact could affect the Vulcano
693 community and surrounding islands at multiple scales.
694 In such a scenario, an effort will be needed to identify the possible precursors of hydrothermal
695 eruptions, not only considering the "classical" geochemical (Chiodini et al. 1995; Capasso et al. 1996;
696 Granieri et al. 2006) and in situ geophysical (Montalto 1996; Fournier and Jolly 2014; Hurst et al.
697 2014; Honda et al. 2018) monitoring, but also considering the opportunities provided by the new and
698 advanced remote sensing techniques (Kobayashi 2018; Kobayashi et al. 2018).
699

Conclusions

Deposits related to the blast phase of the BdC eruption show close similarities with those recently produced at Te Maari-Tongariro (2012) and Ontake (2014) volcanoes, such as the lithic nature of the components, moderate volume of the emitted products and the strong directionality of the eruptive jets (ballistic blocks and dilute PDCs). Despite the difficulties of comparing the BdC eruption with recent events which were directly observed, the reconstructed eruptive sequence displays similar features, with a laterally-directed, fines-depleted blast followed by a final, central vent eruption. Multiple explosions from fissure-like vents have been observed at both the Te Maari-Tongariro, and Ontake isolated hydrothermal blasts and are also necessary to model the Phase 2a of BdC. In such a scenario, large ballistic blocks (up to 30 cm in diameter) initially at rest can be accelerated up to 200 m/s by drag and pressure forces eventually producing concentrated showers of blocks to distances larger than 2 km from the vent.

The blast phase of the BdC eruption (Phase 2a) was preceded by mild ash emissions (Phases 1a and 1b), accounting for a recognizable precursory phase (probably days before the blast). Precursory phases were reported for the eruption of Zao (1895), Adatara (1900) and Soufrière-Guadeloupe (1976), but not for Te Maari-Tongariro and Ontake. Regardless of the existence of predisposing conditions (increased overpressure due to rapid rise of high-pressure gas masses or rapid decompression due to landslides), the increase in the amount of gas in the hydrothermal system is to be considered to be the overall trigger of these eruptions.

The high permeability of the system and the absence of a lava cap at the summit of the cone suggest that the current conditions at La Fossa are not favourable to generate a BdC-like eruption. Nonetheless, the detailed understanding of the alteration style and intensity, as well as the spatial distribution of lithology within the very shallow (within metres) part in the cone area (e.g., Heap et al. 2017; Mayer et al. 2016, 2017) would yield essential information in relation to eventual future unrest phases. This information should also be accompanied by geophysical/geochemical parameters (deformation, thermal flux, gas flux time series), that might indicate a decrease of permeability and

726 an augmented pore pressure (e.g., Fournier and Jolly, 2014; Honda et al. 2018, KoKobayashi et al.
727 2018).
728 Additional, two eruptions should also be considered. As an example, the temporal coincidence of the
729 BdC event with the Rocche Rosse rhyolitic eruption 12 km away from the La Fossa cone is closely
730 reminiscent of the contemporaneity of events that occurred at Tarawera and the Waiotapu geothermal
731 vents situated 10 km apart. Such a contemporaneity of magmatic and hydrothermal events possibly
732 indicates that the activation of regional faults could be an important factor facilitating the rise of high-
733 pressure masses of gas through sudden increase of permeability along the fault plane. In this sense,
734 we emphasize the importance of geophysical parameters in indicating an increase or decrease in
735 permeability and/or of seismic activity.
736

Appendix A. Eulerian-Eulerian model for the gas-pyroclasts mixture

The Eulerian-Eulerian multiphase flow model formulation has been modified from Neri et al. (2003) for one single particulate class, representing fine ash. For the two-phase gas-particle mixture, the following transport equations for mass, momentum and energy are solved. All symbols and units are defined in Appendix D.

Mass equations

$$\begin{aligned} \frac{\partial(\alpha_g \rho_g)}{\partial t} + \nabla \cdot (\alpha_g \rho_g \mathbf{U}_g) &= 0 \\ \frac{\partial(\alpha_s \rho_s)}{\partial t} + \nabla \cdot (\alpha_s \rho_s \mathbf{U}_s) &= 0 \end{aligned}$$

Momentum equations

Because particle-particle collisions are neglected (see below), only the gas pressure term is included in the particle momentum equation (Gidaspow's Model A, 1994).

$$\begin{aligned} \frac{\partial}{\partial t}\left[\alpha_g \rho_g \mathbf{U}_g\right] \quad & + \nabla \cdot \left[\alpha_g \rho_g \mathbf{U}_g \mathbf{U}_g\right] = \\ & = -\alpha_g \nabla P - \nabla \cdot (\alpha_g \rho_g \mathbf{T}_g) + \alpha_g \rho_g \mathbf{g} + D_{gs}(\mathbf{U}_s - \mathbf{U}_g) \end{aligned}$$

$$\begin{aligned} \frac{\partial}{\partial t}\left[\alpha_s \rho_s \mathbf{U}_s\right] \quad & + \nabla \cdot \left[\alpha_s \rho_s \mathbf{U}_s \mathbf{U}_s\right] = \\ & = -\alpha_s \nabla P - \nabla \cdot (\alpha_s \rho_s \mathbf{T}_s) + \alpha_s \rho_s \mathbf{g} - D_{gs}(\mathbf{U}_s - \mathbf{U}_g) \end{aligned}$$

Energy equations

The total energy of the i-th phase is defined as the sum of the specific internal e_i and kinetic k_i energy ($k = \frac{1}{2}\mathbf{U}^2$). The work done by gravity and by the drag force is neglected in both balances. Heat conductivity terms are neglected for particles when focusing on the dilute flow regime.

$$\begin{aligned} \frac{\partial}{\partial t}\left[\alpha_g \rho_g (e_g + k_g)\right] \quad & + \nabla \cdot \left[\alpha_g \rho_g (e_g + k_g) \mathbf{U}_g\right] = \\ & = -\nabla \cdot (\alpha_g \mathbf{q}_g) - \left[p \frac{\partial \alpha_g}{\partial t} + \nabla \cdot (\alpha_g \mathbf{U}_g p)\right] + K_{ht}(T_s - T_g) \end{aligned}$$

$$\frac{\partial}{\partial t}[\alpha_s \rho_s (e_s + k_s)] \quad + \nabla \cdot [\alpha_s \rho_s (e_s + k_s) \mathbf{U}_s] =$$
$$= -\left[P \frac{\partial \alpha_s}{\partial t} + \nabla \cdot (\alpha_s \mathbf{U}_s P) \right] + K_{ht}(T_g - T_s)$$

Closure equations

The two phases are treated as interpenetrating continua. Their volume fractions obey the closure equation:

$$\alpha_g + \alpha_s = 1$$

The thermal equation of state of the gas phase is that of perfect gases. Particle density is constant.

$$\rho_g = \rho_g(P, T_g)$$
$$\rho_s = \text{constant}$$

The frictional and collisional momentum dissipation terms in the particle stress tensors are neglected because they are negligible in the mixture expansion phase and in the dilute regime of pyroclastic flow propagation (Esposti Ongaro et al. 2016). Although they can be important in the basal layer and in the stopping regime of pyroclastic flow emplacement, we have neglected them to speed computation up. Stress terms have been switched on in a couple of runs to ensure that their effect was negligible on large-scale dynamics. On the contrary, turbulent sub-grid stress terms have always been included. For both the gas and particles, the stress tensor is written in a Newtonian form:

$$\mathbf{T}_\mathrm{i} = -2\mu_{\mathrm{eff}} \mathbf{S}_\mathrm{i} - \lambda_\mathrm{i} (\nabla \cdot \mathbf{U}_\mathrm{i}) \mathbf{I}$$
$$\mathbf{S}_\mathrm{i} = \frac{1}{2}\left(\nabla \mathbf{U}_\mathrm{i} + \nabla \mathbf{U}_\mathrm{i}^{\mathrm{T}}\right) - \frac{1}{3}(\nabla \cdot \mathbf{U}_\mathrm{i}) \mathbf{I}$$

where the subscript (i) indicates either gas or particles and ν_{eff} is the effective viscosity coefficient ($\mu_{\mathrm{eff}}=\mu+\mu_{\mathrm{turb}}$), and is the sum of the molecular/granular viscosity μ (equal to 1.84×10^{5} Pa s, for gas, and to zero for particles) and the turbulent (subgrid) turbulent coefficient.

The heat flux is expressed through Fourier's law, for both gas and particles:

$$\mathbf{q}_\mathrm{i} = -\rho_i \left(D_i + \frac{\nu_{\mathrm{turb}}}{\mathrm{Pr}} \right) \frac{C_{P,i}}{C_{V,i}} \nabla e_\mathrm{i}$$

where Pr is the turbulent Prandtl' number, set equal to 0.7 for gas and 1 for particles and $\nu_{\mathrm{turb}}=\mu_{\mathrm{turb}}/\rho_\mathrm{i}$.

778 Finally, the gas-particle drag coefficient D_{gs} is expressed by the Ergun-Wen-Yu law, whereas the gas-
779 particle heat transfer coefficient K_{ht} is expressed by the Ranz-Marshall law. We refer to Neri et al.
780 (2003) for such details.

781 The Eulerian-Eulerian model is solved by means of a segregated, semi-implicit solution algorithm
782 implemented in the twoPhaseEulerFoam application of OpenFOAM (www.openfoam.org, version
783 4.1). The original solver has been modified by the authors to account for atmospheric vertical
784 stratification.

785 **Appendix B. Lagrangian model for ballistics**
786

787 The numerical solver adopted in this work is based on a Lagrangian approach for the larger clasts (de'
788 Michieli Vitturi et al. 2010; Del Bello et al. 2017), using the KinematicCloud class implemented in
789 OpenFOAM. In the present application, the Lagrangian trajectories are calculated by imposing a one-
790 way coupling with the continuous phases (gas and fine particles), i.e., Lagrangian particles are
791 influenced by the fluid field but their mass fraction is low enough to neglect their influence on the
792 fluid.
793 In the Lagrangian formulation, trajectories are obtained by integrating, for each particle P with mass
794 m_p and velocity $\mathbf{U}_p$, the Newton equation of motion expressing acceleration of a particle as a function
795 of the sum of the forces acting on the particle:
796

797 $$m_p \frac{d\mathbf{U}_p}{dt} = \sum \mathbf{F}_p$$

798

799 In this application, we considered the steady state fluid-particle drag $\mathbf{F}_D$, the pressure gradient $\mathbf{F}_G$ and
800 the body force $\mathbf{F}_B$ (i.e., gravity). Virtual mass, Magnus and Basset forces are neglected as their
801 magnitude is usually much smaller (de' Michieli Vitturi et al. 2010):

802 $$\sum \mathbf{F}_p = \mathbf{F}_D + \mathbf{F}_P + \mathbf{F}_G$$

803

804 In dilute flows, such as those of interest in this work, the dominant force acting on the particles
805 (besides gravity $\mathbf{F}_G = m_P \mathbf{g}$) is the drag exerted by the fluid phase, expressed by:

806 $$\mathbf{F}_D = \frac{1}{2}\rho_C |\mathbf{U}_C - \mathbf{U}_P| (\mathbf{U}_C - \mathbf{U}_P) C_D \pi \left(\frac{D_P}{2}\right)^2$$

807

808 In this expression, D_P is the particle diameter, whereas the subscripts C and P indicate the continuous
809 phase and the particle, respectively. For the drag coefficient C_D, we adopt the same expression used
810 by Neri et al. (2003):

811

812 $$C_D = \frac{24}{\mathrm{Re}}(1 + 0.15\ \mathrm{Re}^{0.687})$$

813

814 valid up to Re=1000, with the particle Reynolds number Re defined as:

815

816 $$\mathrm{Re} = \frac{\rho_C |\mathbf{U}_C - \mathbf{U}_P| D_P}{\mu_C}$$

817

818 where ρ_C is the density of the carrier phase, $\mathbf{U}_C$ is its velocity and μ_C is the dynamic viscosity.
819 De' Michieli Vitturi et al. (2010) already demonstrated that, in the initial stages of a Vulcanian
820 eruption, the pressure gradient terms are of the same order of magnitude as the drag term. In our work,
821 we thus included the pressure gradient in the Lagrangian equations and noticed that this term is a
822 fundamental one to correctly estimate the ballistic ranges. Neglecting the pressure gradient entails a
823 decrease of the maximum distance reached by 30 cm particles by about 25% (i.e., from 1.90 to 1.45
824 km).
825 The pressure gradient force is written as:

826 $$\mathbf{F}_G = -\frac{m_P}{\rho_P}\nabla P$$

827

828 All force terms are first computed at the centers of the computational cells and then linearly
829 interpolated at the particle position to update particle velocity. Finally, new particle positions are
830 obtained by integration of the velocity:

831 $$\frac{d\mathbf{x}_p}{dt} = \mathbf{U}_p$$

832 **Appendix C. Topographic boundary conditions and numerical mesh**
833

834 The Digital Elevation Model (DEM) represents the present topography of the Vulcano island, with
835 the crater filled up to the rim (Fig. C1a). At time *t=0*, the eruptive mixture is confined within a shallow
836 fissure excavated in the crater area. To reproduce the observed spreading in East-Southeast directions,
837 the fissure was oriented N35°E, the inner profile was asymmetrically opened towards Southeast (Fig.
838 C1b) and ballistic particles where located along the southeastern margin of the fissure. It is worth
839 remarking that asymmetric ballistic launch can be produced in natural systems by an oriented fissure
840 or an inclined jet but, in our application, it was not possible to test such a geometry. In any case, our
841 study demonstrates that ballistic particles ejected towards the East-Southeast can reach, with the
842 selected initial conditions, the observed ranges.
843 The DEM was converted in STL format and the computational grid was adapted to the topography
844 by using the snappyHexMesh utility, implemented in OpenFOAM 4.1. The computational domain is
845 extended 4.6 km in the *x* direction (West-East), 4.3 km in the *y* direction (South-North) and 2.5 km
846 vertically. An initial coarse, rectilinear uniform mesh (with 100 m resolution in all directions) was
847 refined in two steps, to obtain a 25-m resolution at the ground surface. Two terrain-following layers
848 were then added, with an average vertical resolution of 10 m. Such a local refinement allowed to have
849 enough resolution to resolve the large-scale features of dilute and thick pyroclastic density currents
850 (Esposti Ongaro et al. 2016), while keeping affordable the number of computational cells (~280,000)

and the simulation time (~3 hours) for simulation on a Intel i5 4-cores (3.2 GHz) PC.

Appendix D. List of mathematical symbols

Symbols	Meaning	Dimensions
$\boldsymbol{\alpha}$	Volume fraction	
$\boldsymbol{\rho}$	Density	[kg][m]$^{-3}$
$\mathbf{U}$	Velocity	[m][s]$^{-1}$
$\boldsymbol{P}$	Pressure	[Pa]=[kg][m]$^{-1}$[s]$^{-2}$
$\boldsymbol{T}$	Temperature	[K]
$\boldsymbol{e}$	Specific thermal energy	[J][kg]$^{-1}$=[m]^{2}[s]$^{-2}$
$\boldsymbol{k}$	Specific kinetic energy	[m]^{2}[s]$^{-2}$
$\mathbf{T}$	Stress tensor	[Pa]
$\mathbf{q}$	Energy flux	[kg][s]$^{-3}$
$\mathbf{S}$	Deviatoric tensor	[s]$^{-1}$
$\mathbf{g}$	Gravity acceleration	[m][s]$^{-2}$
$\boldsymbol{D_{gs}}$	Gas-particle Drag coefficient	[kg][m]$^{-3}$[s]$^{-1}$
$\boldsymbol{K_{ht}}$	Gas-particle Heat exchange coefficient	[kg][m]$^{-1}$[s]$^{-3}$[K]$^{-1}$
$\boldsymbol{\nu}$	Kinematic viscosity coefficient	[m]^{2}[s]$^{-1}$
$\boldsymbol{\mu}$	Dynamic viscosity coefficient	[Pa][s]
$\boldsymbol{\lambda}$	Secondary dynamic viscosity coefficient	[Pa][s]
$\boldsymbol{D_i}$	Heat diffusion coefficient for phase i	[m]^{2}[s]$^{-1}$
$\boldsymbol{C_{P,i}}$	Specific heat at constant pressure for phase i	[J][kg]$^{-1}$[K]$^{-1}$
$\boldsymbol{C_{V,i}}$	Specific heat at constant volume for phase i	[J][kg]$^{-1}$[K]$^{-1}$
$\boldsymbol{R}$	Specific gas constant	[J][kg]$^{-1}$[K]$^{-1}$
$\boldsymbol{n}$	Gas mass fraction	
$\boldsymbol{\phi}$	Porosity (gas volume fraction) of the exploding mixture	
$\boldsymbol{m_p}$	Ballistic particle mass	[kg]
$\mathbf{F}$	Force acting on a ballistic particle	[kg][m][s]$^{-2}$
$\mathbf{Re}$	Reynolds number	
$\mathbf{Pr}$	Prandtl' number	
Subscripts		
$\mathbf{g}$	Gas phase	
$\mathbf{s}$	Solid particulate phase	

Acknowledgments

C. Bonadonna was supported by the Swiss National Science Foundation (subside # 200021-129997). The authors are grateful to R. Fusillo (Univ. Bristol) for assistance during the fieldwork. F. di Traglia was supported by a post-doc fellowship founded by the "Università degli Studi di Firenze – Ente Cassa di Risparmio di Firenze" (D.R. n. 127804 (1206), 2015). The authors are grateful to the "INGV-Sezione di Palermo" staff, especially to P. Madonia, for the logistic support at the "M. Carapezza" Volcanological Observatory (Island of Vulcano) during field activities. L. Gurioli and C. Montanaro are acknowledged for their careful and constructive reviews which greatly enhanced the quality of the manuscript, and Pierre-Simon Ross for editorial handling.

867 **References**

868 Albert PG, Tomlinson EL, Smith VC, Di Traglia F, Pistolesi M, Morris A, Donato P, De Rosa R,
869 Sulpizio R, Keller J, Rosi M (2017) Glass geochemistry of pyroclastic deposits from the
870 Aeolian Islands in the last 50 ka: A proximal database for tephrochronology. J Volcanol
871 Geotherm Res 336:81-107.

872 Arrighi S, Tanguy JC, Rosi M (2006) Eruptions of the last 2200 years at Vulcano and Vulcanello
873 (Aeolian Islands, Italy) dated by high-accuracy archeomagnetism. Phys Earth Planet Int
874 159:225–233.

875 Barberi F, Bertagnini A, Landi P, Principe C (1992) A review on phreatic eruptions and their
876 precursors. J Volcanol Geotherm Res 52:231–246.

877 Belousov A (1996) Deposits of the 30 March 1956 directed blast at Bezymianny volcano, Kamchatka,
878 Russia. Bull Volcanol 57(8):649-662.

879 Belousov A, Voight B, Belousova M (2007) Directed blasts and blast-generated pyroclastic density
880 currents: a comparison of the Bezymianny 1956, Mount St Helens 1980, and Soufrière Hills,
881 Montserrat 1997 eruptions and deposits. Bull Volcanol 69:701.

882 Bescoby D, Barclay J, Andrews J (2008) Saints and Sinners: a tephrochronology for Late Antique
883 landscape change in Epirus from the eruptive history of Lipari, Aeolian Islands. J Archeol Sci
884 35:2574–2579.

885 Biass S, Bonadonna C, Di Traglia F, Pistolesi M, Rosi M, Lestuzzi P (2016a) Probabilistic evaluation
886 of the physical impact of future tephra fallout events for the Island of Vulcano, Italy. Bull
887 Volcanol 78:1-22.

888 Biass S, Falcone JL, Bonadonna C, Di Traglia F, Pistolesi M, Rosi M, Lestuzzi P (2016b) Great Balls
889 of Fire: A probabilistic approach to quantify the hazard related to ballistics—A case study at
890 La Fossa volcano, Vulcano Island, Italy. J Volcanol Geotherm Res 325:1-14.

891 Biggs J, Robertson E, Cashman K (2016) The lateral extent of volcanic interactions during unrest and
892 eruption. Nature Geoscience 9(4):308.

893 Blanco-Montenegro I, De Ritis R, Chiappini M (2006) Imaging and modelling the subsurface
894 structure of volcanic calderas with high-resolution aeromagnetic data at Vulcano (Aeolian
895 Islands, Italy). Bull Volcanol 69:643–659
896 Bonadonna C, Costa A (2012) Estimating the volume of tephra deposits: a new simple strategy.
897 Geology 40:415–418.
898 Boudon G, Lajoie J (1989) The 1902 Peléean deposits in the Fort Cemetery of St. Pierre, Martinique:
899 A model for the accumulation of turbulent nuees ardentes. In: G. Boudon and A. Gourgaud
900 (Editors), Mount Pelée. J Volcanol Geotherm Res 38:113-130
901 Breard ECP, Lube G, Cronin SJ, Fitzgerald R, Kennedy B, Scheu B, Montanaro C, White JDL, Tost
902 M, Procter JN, Moebis A (2014) Using the spatial distribution and lithology of ballistic blocks
903 to interpret eruption sequence and dynamics: August 6 2012 Upper Te Maari eruption, New
904 Zealand. J Volcanol Geotherm Res 286:373-386.
905 Breard ECP, Lube G, Cronin SJ, Valentine GA (2015) Transport and deposition processes of the
906 hydrothermal blast of the 6 August 2012 Te Maari eruption, Mt. Tongariro. Bull Volcanol
907 77:100.
908 Brissette FP, Lajoie J (1990) Depositional mechanics of turbulent nuees ardentes (surges) from their
909 grain sizes. Bull Volcanol 53:60-66.
910 Browne P, Lawless J. (2001) Characteristics of hydrothermal eruptions, with examples from New
911 Zealand and elsewhere. Earth-Science Reviews 52:299-331.
912 Bullock LA, Gertisser R, O'driscoll B (2018) Emplacement of the Rocche Rosse rhyolite lava flow
913 (Lipari, Aeolian Islands). Bull Volcanol 80(5):48.
914 Burns FA, Bonadonna C, Pioli L, Cole PD, Stinton A (2017) Ash aggregation during the 11 February
915 2010 partial dome collapse of the Soufrière Hills Volcano, Montserrat. J Volcanol Geotherm
916 Res 335:92-112.
917 Calvache VML, Williams SN (1992) Lithic-dominated pyroclastic flows at Galeras volcano,
918 Colombia — an unrecognised volcanic hazard. Geology 20:539–542.

919 Capaccioni B, Coniglio S (1995) Varicolored and vesiculated tuffs from La Fossa volcano, Vulcano
920 Island (Aeolian Archipelago, Italy): evidence of syndepositional alteration processes. Bull
921 Volcanol 57:61-70
922 Capasso G, Favara R, Inguaggiato S (1997) Chemical features and isotopic composition of gaseous
923 manifestations on Vulcano Island, Aeolian Islands, Italy: an interpretative model of fluid
924 circulation. Geochim Cosmochim Acta 61(16):3425-3440.
925 Capasso G, Federico C, Madonia P, Paonita A (2014) Response of the shallow aquifer of the volcano-
926 hydrothermal system during the recent crises at Vulcano Island (Aeolian Archipelago, Italy).
927 J Volcanol Geotherm Res 273:70-80.
928 Caron B, Siani G, Sulpizio R, Zanchetta G, Paterne M, Santacroce R, Tema E, Zanella E (2012) Late
929 Pleistocene to Holocene tephrostratigraphic record from the Northern Ionian Sea. Mar Geol
930 311-314:41-51.
931 Carn SA, Watts RB, Thompson G, Norton GE (2004) Anatomy of a lava dome collapse: the 20 March
932 2000 event at Soufrière Hills Volcano, Montserrat. J Volcanol Geotherm Res 131:241-264.
933 Cerminara M, Esposti Ongaro T, Berselli LC (2016) ASHEE-1.0: a compressible, equilibrium-
934 Eulerian model for volcanic ash plumes. Geosci Model Dev 9:697–730.
935 Chiodini G, Cioni R, Marini L, Panichi C (1995) Origin of the fumarolic fluids of Vulcano Island,
936 Italy and implications for volcanic surveillance. Bull Volcanol 57(2):99-110.
937 Chiodini G, Frondini F, Raco B (1996) Diffuse emission of CO 2 from the Fossa crater, Vulcano
938 Island (Italy). Bull Volcanol 58(1):41-50.
939 Chretien S, Brousse R (1989) Events preceding the great eruption of 8 May, 1902 at Mount Pelée,
940 Martinique. J Volcanol Geotherm Res 38:67-75
941 Clarke AB, Neri A, Voight B, Macedonio G, Druitt TH (2002) Computational modelling of the
942 transient dynamics of the August 1997 Vulcanian explosions at Soufriere Hills Volcano,
943 Montserrat: influence of initial conduit conditions on near-vent pyroclastic dispersal. Mem-
944 Geol Soc London, 21:319-348.

945 Cortese M, Frazzetta G, La Volpe L (1986) Volcanic history of Lipari (Aeolian Islands, Italy) during
946 the last 10,000 years. J Volcanol Geotherm Res 27:117–133.
947 De Astis G, Dellino P, La Volpe L, Lucchi F, Tranne CA (2006) Geological map of the Vulcano Island.
948 Litografia artistica cartografica, Firenze.
949 De Astis G, Lucchi F, Dellino P, La Volpe L, Tranne CA, Frezzotti ML, Peccerillo A (2013) Geology,
950 volcanic history and petrology of Vulcano (central Aeolian archipelago). Geol Soc Lond Mem
951 37:281–349
952 De Fiore O (1922) Vulcano (Isole Eolie). In: Friedlaender, I. (Ed.), Rivista Vulcanologica (Suppl. 3):
953 1–393.
954 de' Michieli Vitturi M, Neri A, Esposti Ongaro T, Lo Savio S, Boschi E (2010) Lagrangian modeling
955 of large volcanic particles: Application to Vulcanian explosions. J Geophys Res SE 115(B8).
956 Dade B, Huppert H (1998) Long-runout rockfalls. Geol 26:803–806.
957 Davì M, De Rosa R, Donato P, Vetere F, Barca D, Cavallo A (2009a) Magmatic Evolution and
958 plumbing system of ring-fault volcanism: the Vulcanello Peninsula (Aeolian Islands, Italy).
959 Eur J Mineral 21:1009-1028.
960 Davì M, De Rosa R, Barca D (2009b) A LA-ICP-MS study of minerals in the Rocche Rosse magmatic
961 enclaves: Evidence of a mafic input triggering the latest silicic eruption of Lipari Island
962 (Aeolian Arc, Italy). J Volcanol Geotherm Res 182:45-56.
963 Davì M, De Rosa R, Donato P, Sulpizio R (2011) The Lami pyroclastic succession (Lipari, Aeolian
964 Islands): A clue for unravelling the eruptive dynamics of the Monte Pilato rhyolitic pumice
965 cone. J Volcanol Geotherm Res 201:285-300.
966 Del Bello E, Taddeucci J, de' Michieli Vitturi M, Scarlato P, Andronico D, Scollo S, Kueppers U,
967 Ricci T (2017) Effect of particle volume fraction on the settling velocity of volcanic ash
968 particles: insights from joint experimental and numerical simulations. Sci Rep 7:39620.
969 Dellino P, La Volpe L (1995) Fragmentation versus transportation mechanisms in the pyroclastic
970 sequence of Monte Pilato-Rocche Rosse (Lipari, Italy). J Volcanol Geotherm Res 64:211–231.

971 Dellino P, De Astis G, La Volpe L, Mele D, Sulpizio, R (2011) Quantitative hazard assessment of
972 phreatomagmatic eruptions at Vulcano (Aeolian Islands, Southern Italy), as obtained by
973 combining stratigraphy, event statistics and physical modelling. J Volcanol Geotherm Res
974 201:364-384
975 Di Traglia F, Pistolesi M, Rosi M, Bonadonna C, Fusillo R, Roverato M (2013) Growth and erosion:
976 volcanic geology and morphological evolution during the last 1000 years of La Fossa (Island
977 of Vulcano, Southern Italy). Geomorph 194:94-107.
978 Diliberto IS (2017) Long-term monitoring on a closed-conduit volcano: A 25 year long time-series of
979 temperatures recorded at La Fossa cone (Vulcano Island, Italy), ranging from 250° C to 520°
980 C. J Volcanol Geotherm Res 346:151-160.
981 Erfurt-Cooper P (2011) Geotourism in volcanic and geothermal environments: playing with fire?.
982 Geoheritage, 3(3):187-193.
983 Esposti Ongaro T, Clarke AB, Voight B, Neri A, Widiwijayanti C (2012) Multiphase flow dynamics
984 of pyroclastic density currents during the May 18, 1980 lateral blast of Mount St. Helens. J
985 Geophys Res SE 117(B6).
986 Esposti Ongaro T, Orsucci S, Cornolti F (2016) A fast, calibrated model for pyroclastic density
987 currents kinematics and hazard. J Volcanol Geoth Res 327:257-272.
988 Federico C, Capasso G, Paonita A, Favara R (2010) Effects of steam-heating processes on a stratified
989 volcanic aquifer: Stable isotopes and dissolved gases in thermal waters of Vulcano Island
990 (Aeolian archipelago). J Volcanol Geotherm Res 192:178-190.
991 Fitzgerald RH, Tsunematsu K, Kennedy BM, Breard ECP, Lube G, Wilson TM, Jolly AD, Pawson J,
992 Rosenberg MD, Cronin SJ (2014) The application of a calibrated 3D ballistic trajectory model
993 to ballistic hazard assessments at Upper Te Maari, Tongariro. J Volcanol Geoth Res 286:248-
994 262.
995 Fitzgerald RH, Kennedy BM, Wilson TM, Leonard GS, Tsunematsu K, Keys H (2017) The
996 Communication and Risk Management of Volcanic Ballistic Hazards. Springer Berlin

997 Heidelberg, pp. 1 – 27.
998 Forni F, Lucchi F, Peccerillo A, Tranne CA, Rossi PL, Frezzotti ML (2013) Stratigraphy and
999 geological evolution of the Lipari volcanic complex (central Aeolian archipelago). Geol Soc
1000 London Mem 37:213-279.
1001 Fournier N, Jolly AD (2014) Detecting complex eruption sequence and directionality from high-rate
1002 geodetic observations: The August 6, 2012 Te Maari eruption, Tongariro, New Zealand. J
1003 Volcanol Geoth Res 286:387-396.
1004 Frazzetta G, La Volpe L, Sheridan MF (1983) Evolution of the La Fossa cone, Vulcano. J Volcanol
1005 Geotherm Res 17:329–360.
1006 Frazzetta G, Gillot PY, La Volpe L, Sheridan M.F (1984) Volcanic hazards at La Fossa of Vulcano:
1007 data from the last 6000 years. Bull Volcanol 47:105–124.
1008 Fujinawa A, Ban M, Ohba T, Kontani K, Miura K (2008) Characterization of low-temperature
1009 pyroclastic surges that occurred in the northeastern Japan arc during the late 19th century. J
1010 Volcanol Geotherm Res 178:113-130
1011 Fulignati P, Gioncada A, Sbrana A (1998) Geologic model of the magmatic-hydrothermal system of
1012 Vulcano (Aeolian Island, Italy). Mineral Petrol 62:195–222.
1013 Fulignati P, Gioncada A, Costa S, Di Genova D, Di Traglia F, Pistolesi M (2018) Magmatic sulfide
1014 immiscibility at an active magmatic-hydrothermal system: The case of La Fossa (Vulcano,
1015 Italy). Volcanol Geotherm Res 358:45-75.
1016 Fusillo R, Di Traglia F, Gioncada A, Pistolesi M, Wallace PJ, Rosi M (2015) Deciphering post-caldera
1017 volcanism: insight into the Vulcanello (Island of Vulcano, Southern Italy) eruptive activity
1018 based on geological and petrological constraints. Bull Volcanol 77:76.
1019 Galderisi A, Bonadonna C, Delmonaco G, Ferrara FF, Menoni S, Ceudech A, Biass S, Frischknecht
1020 C, Manzella I, Minucci G, Gregg C (2013) Vulnerability Assessment and Risk Mitigation:
1021 The Case of Vulcano Island, Italy, Landslide Science and Practice, Volume 7: Social and
1022 Economic Impact and Policies, Springer Berlin Heidelberg 55-64.

1023 Gardner CA, White RA (2002) Seismicity, gas emission and deformation from 18 July to 25
1024 September 1995 during the initial phreatic phase of the eruption of Soufriere Hills Volcano,
1025 Montserrat. In: Druitt, T.H., Kokelaar, B.P. (Eds.), The eruption of Soufriere Hills Volcano,
1026 Montserrat from 1995 to 1999. Geol Soc London Mem 21:567–581.
1027 Germanovich LN, Lowell RP (1995) The mechanism of phreatic eruptions. J Geophys Res 100:8417–
1028 8434.
1029 Gidaspow D (1994) Multiphase flow and fluidization: continuum and kinetic theory descriptions.
1030 Academic press.
1031 Gioncada A, Sbrana A (1991) La Fossa caldera. Vulcano: inferences from deep drillings. Acta
1032 Vulcanol 1:115-125.
1033 Gioncada A, Mazzuoli R, Bisson M, Pareschi MT (2003) Petrology of volcanic products younger
1034 than 42 ka on the Lipari–Vulcano complex (Aeolian Islands, Italy): an example of volcanism
1035 controlled by tectonics. J Volcanol Geotherm Res 122:191-220.
1036 Granieri D, Carapezza ML, Chiodini G, Avino R, Caliro S, Ranaldi M, Ricci T, Tarchini L (2006)
1037 Correlated increase in CO2 fumarolic content and diffuse emission from La Fossa crater
1038 (Vulcano, Italy): Evidence of volcanic unrest or increasing gas release from a stationary deep
1039 magma body?. Geophys Res Lett, 33(13).
1040 Gurioli L, Zanella E, Gioncada A, Sbrana A (2012) The historic magmatic-hydrothermal eruption of
1041 the Breccia di Commenda, Vulcano, Italy. Bull Volcanol 74:1235–1254.
1042 Harris AJ, Stevenson DS (1997) Thermal observations of degassing open conduits and fumaroles at
1043 Stromboli and Vulcano using remotely sensed data. J Volcanol Geoth Res 76(3-4): 175-198.
1044 Hincks TK, Komorowski J-C, Sparks SR, Aspinall WP (2014) Retrospective analysis of uncertain
1045 eruption precursors at La Soufrière volcano, Guadeloupe, 1975–77: volcanic hazard
1046 assessment using a Bayesian belief network approach. J Appl Volcanol 3:3.
1047 Hayashi JN, Self S (1992) A comparison of pyroclastic flow and debris avalanche mobility. J.
1048 Geophys. Res. Solid Earth 97(B6):9063-9071.

1049 Heap MJ, Kennedy BM, Farquharson JI, Ashworth J, Mayer K, Letham-Brake M, Reuschlé T, Albert
1050 Gilg H, Scheu B, Lavallée Y, Siratovich P, Cole J, Jolly AD, Baud P, Dingwell DB (2017) A
1051 multidisciplinary approach to quantify the permeability of the Whakaari/White Island
1052 volcanic hydrothermal system (Taupo Volcanic Zone, New Zealand). J Volcanol Geoth Res
1053 332:88-108,
1054 Heggie, T W (2009) Geotourism and volcanoes: health hazards facing tourists at volcanic and
1055 geothermal destinations. Travel medicine and infectious disease, 7(5):257-261.
1056 Heiken G, Crowe B, McGetchin T, West F, Eichelberger J, Bartram D, Peterson R, Wohletz K (1980)
1057 Phreatic eruption clouds: the activity of la Soufriére de Guadeloupe, F.W.I., August-October.
1058 Bull Volcanol 43:383-395.
1059 Hoblitt RP (2000) Was the 18 May 1980 lateral blast at Mt St Helens the product of two explosions?
1060 Phil Trans Royal Soc London 358:1639–1661.
1061 Honda R, Yukutake Y, Morita Y, Sakai SI, Itadera K, Kokubo K (2018) Precursory tilt changes
1062 associated with a phreatic eruption of the Hakone volcano and the corresponding source
1063 model. Earth, Planets and Space 70(1):117.
1064 Houghton BF, Swanson DA, Carey RJ, Rausch J, Sutton AJ (2011) Pigeonholing pyroclasts: Insights
1065 from the 19 March 2008 explosive eruption of Kīlauea volcano. Geology 39:263-266.
1066 Hurst T, Jolly AD, Sherburn S (2014) Precursory characteristics of the seismicity before the 6 August
1067 2012 eruption of Tongariro volcano, North Island, New Zealand. J Volcanol Geotherm Res
1068 286:294-302.
1069 Jolly AD, Jousset P, Lyons JJ, Carniel R, Fournier N, Fry B, Miller C (2014) Seismo-acoustic
1070 evidence for an avalanche driven phreatic eruption through a beheaded hydrothermal system:
1071 An example from the 2012 Tongariro eruption. J Volcanol Geotherm Res 286:331-347.
1072 Kato A, Terakawa T, Yamanaka Y, Maeda Y, Horikawa S, Matsuhiro K, Okuda T (2016) Preparatory
1073 and precursory processes leading up to the 2014 phreatic eruption of Mount Ontake, Japan.
1074 Earth, Planets and Space 67:111.

1075 Keller J (1980) The island of Vulcano. Rend Soc Italian Miner Petrol 36:369–414.
1076 Kobayashi T (2018) Locally distributed ground deformation in an area of potential phreatic eruption,
1077 Midagahara volcano, Japan, detected by single-look-based InSAR time series analysis. J
1078 Volcanol Geotherm Res 357:213-223.
1079 Kobayashi T, Morishita Y, Munekane H (2018) First detection of precursory ground inflation of a
1080 small phreatic eruption by InSAR. Earth Planet Sci Lett 491:244-254.
1081 Lajoie J, Boudon G, Bourdier JL (1989) Depositional mechanics of the 1902 pyroclastic nuee ardente
1082 deposits of Mt. Pelee, Martinique. J Volcanol Geotherm Res 38:131-142.
1083 Le Guern F, Bernard A, Chevrier RM (1980) Soufriere of Guadeloupe 1976–1977 eruption-mass and
1084 energy transfer and volcanic health hazards. Bull Volcanol 43:577–593.
1085 Lube G, Breard EC, Cronin SJ, Procter JN, Brenna M, Moebis A, Pardo N, Stewart RB, Jolly A,
1086 Fournier N (2014) Dynamics of surges generated by hydrothermal blasts during the 6 August
1087 2012 Te Maari eruption, Mt. Tongariro, New Zealand. J Volcanol Geotherm Res 286:348-366.
1088 Maeno F, Nakada S, Oikawa T, Yoshimoto M, Komori J, Ishizuka Y, Takeshita Y, Shimano T, Kaneko
1089 T, Nagai M (2016) Reconstruction of a phreatic eruption on 27 September 2014 at Ontake
1090 volcano, central Japan, based on proximal pyroclastic density current and fallout deposits.
1091 Earth, Planets and Space 68:1-20.
1092 Mandarano M, Paonita A, Martelli M, Viccaro M, Nicotra E, Millar IL (2016) Revealing magma
1093 degassing below closed-conduit active volcanoes: Geochemical features of volcanic rocks
1094 versus fumarolic fluids at Vulcano (Aeolian Islands, Italy). Lithos 248:272-287.
1095 Mannen K, Yukutake Y, Kikugawa G, Harada M, Itadera K, Takenaka J (2018) Chronology of the
1096 2015 eruption of Hakone volcano, Japan: geological background, mechanism of volcanic
1097 unrest and disaster mitigation measures during the crisis. Earth, Planets and Space 70:1-26.
1098 Mayberry GC, Rose WI, Bluth GJS (2002) Dynamics of volcanic and meteorological clouds
1099 produced on 26 December (Boxing Day) 1997 at Soufriere Hills Volcano, Montserrat. In:
1100 Druitt, T.H., Kokelaar, B.P. (Eds.), The Eruption of Soufriere Hills Volcano, Montserrat, from

1995 to 1999.Geol Soc London Mem 21:539–555.

Mayer K, Scheu B, Montanaro C, Yilmaz TI, Isaia R, Aßbichler D, Dingwell DB (2016) Hydrothermal alteration of surficial rocks at Solfatara (Campi Flegrei): Petrophysical properties and implications for phreatic eruption processes. J Volcanol Geotherm Res 320:128-143.

Mayer K, Scheu B, Yilmaz TI, Montanaro C, Gilg HA, Rott S, Joseph EP, Dingwell, D. B. (2017) Phreatic activity and hydrothermal alteration in the Valley of Desolation, Dominica, Lesser Antilles. Bull Volcanol 79(12):82.

Marini L, Principe C, Chiodini G, Cioni R, Fytikas M, Marinelli G (1993) Hydrothermal eruptions of Nisyros (Dodecanese, Greece) — past events and present hazard. J Volcanol Geotherm Res 56:71–94.

Mastin LG (1995) Thermodynamics of gas and steam-blast eruptions. Bull Volcanol 57(2):85-98.

McKibbin R, Smith T, Fullard L (2009) Components and Phases: Modelling Progressive Hydrothermal Eruptions. ANZIAM J. 50, 365. https://doi.org/10.1017/S144618110900011X

Mercalli G, Silvestri O (1891) Le eruzioni dell'isola di Vulcano, incominciate il 3 Agosto 1888 e terminate il 22 Marzo 1880. Annali dell'Ufficio Centrale di Meteorologia e Geodinamica 10:1-213.

Miura K, Ban M, Ohba T, Fujinawa A (2012) Sequence of the 1895 eruption of the Zao volcano, Tohoku Japan. J Volcanol Geotherm Res 247:139-157.

Montalto A (1995) Seismic assessment of phreatic-explosion hazard at ‘La Fossa’Volcano (Island of Vulcano, Italy). Natural hazards 11(1):57-73.

Montanaro C, Scheu B, Cronin SJ, Breard EC, Lube G, Dingwell DB (2016a) Experimental estimates of the energy budget of hydrothermal eruptions; application to 2012 Upper Te Maari eruption, New Zealand. Earth Planet Sci Lett 452:281-294.

Montanaro C, Scheu B, Gudmundsson MT, Vogfjörd K, Reynolds HI, Dürig T, Strehlow K, Rott S, Reuschlé T, Dingwell DB (2016b) Multidisciplinary constraints of hydrothermal explosions

based on the 2013 Gengissig lake events, Kverkfjöll volcano, Iceland. Earth Planet Sci Lett 434:308-319.

Montanaro C, Scheu B, Mayer K, Orsi G, Moretti R, Isaia R, Dingwell DB (2016) Experimental investigations on the explosivity of steam-driven eruptions: A case study of Solfatara volcano (Campi Flegrei). J Geophys Res, Solid Earth 121:7996-8014.

Nairn IA, Hedenquist JW, Villamor P, Berryman KR, Shane PA (2005) The ~AD1315 Tarawera and Waiotapu eruptions, New Zealand: contemporaneous rhyolite and hydrothermal eruptions driven by an arrested basalt dike system? Bull Volcanol 67:186-193.

Napoli R, Currenti G (2016) Reconstructing the Vulcano Island evolution from 3D modeling of magnetic signatures. J Volcanol Geother Res 320:40–49.

Neri A, Esposti Ongaro T, Macedonio G, Gidaspow D (2003) Multiparticle simulation of collapsing volcanic columns and pyroclastic flow. J Geophys Res SE 108(B4).

Nicotra E, Giuffrida M, Viccaro M, Donato P, D'Oriano C, Paonita A, De Rosa R (2018) Timescales of pre-eruptive magmatic processes at Vulcano (Aeolian Islands, Italy) during the last 1000 years. Lithos 316-317:347-365.

Ohba T, Taniguchi H, Miyamoto T, Hayashi S, Hasenaka T (2007) Mud plumbing system of an isolated phreatic eruption at Akita Yakeyama volcano, northern Honshu, Japan. J Volcanol Geotherm Res 161:35–46.

Oikawa T, Yoshimoto M, Nakada S, Maeno F, Komori J, Shimano T, Takeshita Y, Ishizuka Y, Ishimine Y (2016) Reconstruction of the 2014 eruption sequence of Ontake Volcano from recorded images and interviews. Earth, Planets and Space 68:79.

Paonita A, Federico C, Bonfanti P, Capasso G, Inguaggiato S, Italiano F, Madonia P, Pecoraino G, Sortino F (2013) The episodic and abrupt geochemical changes at La Fossa fumaroles (Vulcano Island, Italy) and related constraints on the dynamics, structure, and compositions of the magmatic system. Geochim Cosmochim Acta, 120:158-178.

Pardo N, Cronin SJ, Németh K, Brenna M, Schipper CI, Breard E, White JDL, Procter J, Stewart B,

1153 Agustín-Flores J, Moebis A, Zernack A, Kereszturi G, Lube G, Auer A, Neall V, Wallace C
1154 (2014) Perils in distinguishing phreatic from phreatomagmatic ash; insights into the eruption
1155 mechanisms of the 6 August 2012 Mt. Tongariro eruption, New Zealand. J Volcanol Geotherm
1156 Res 286:397-414.
1157 Pistolesi M, Isaia R, Marianelli P, Bertagnini A, Fourmentraux C, Albert PG, Tomlinson EL, Menzies,
1158 MA, Rosi M, Sbrana A (2016) Simultaneous eruptions from multiple vents at Campi Flegrei
1159 (Italy) highlight new eruption processes at calderas: Geology 44:487–490, doi:
1160 10.1130/G37870.1.
1161 Pyle DM (1989) The thickness, volume and grainsize of tephra fall deposits. Bull Volcanol 51:1-15.
1162 Reid ME (2004) Massive collapse of volcano edifices triggered by hydrothermal pressurization.
1163 Geology 32:373-376.
1164 Ritchie LJ, Cole PD, Sparks RSJ (2002) Sedimentology of deposits from the pyroclastic density
1165 current of 26 December 1997 at Soufrière Hills Volcano, Montserrat. Geol Soc London Mem
1166 21:435-456.
1167 Roggensack K, Williams SN, Schaefer SJ, Parnell RA (1996) Volatiles from the 1994 eruptions of
1168 Rabaul: Understanding large caldera systems: Science 273:490–493, doi:10.1126
1169 /science.273.5274.490.
1170 Romagnoli C, Casalbore D, Chiocci FL (2012) La Fossa Caldera breaching and submarine erosion
1171 (Vulcano island, Italy). Mar Geol 303:87-98.
1172 Ruch J, Vezzoli L, De Rosa R, Di Lorenzo R, Acocella V (2016) Magmatic control along a strike-slip
1173 volcanic arc: The central Aeolian arc (Italy). Tectonics 35:407-424.
1174 Sheridan MF (1980) Pyroclastic block flow from the September, 1976, eruption of La Soufrière
1175 volcano, Guadeloupe. Bull Volcanol 43:397-402.
1176 Sheridan MF, Malin MC (1983) Application of computer-assisted mapping to volcanic hazard
1177 evaluation of surge eruptions: Vulcano, Lipari, and Vesuvius. J Volcanol Geotherm Res 17(1-
1178 4):187-202.

1179 Soligo M, De Astis G, Delitala MC, La Volpe L, Taddeucci A, Tuccimei P (2000) Uranium-series
1180 disequilibria in the products from Vulcano Island (Sicily, Italy): isotopic chronology and
1181 magmatological implications. Acta Vulcanologica 12:49–59
1182 Stix J, de Moor JM (2018) Understanding and forecasting phreatic eruptions driven by magmatic
1183 degassing. Earth, Planets and Space 70(1):83.
1184 Strehlow K, Sandri L, Gottsmann JH, Kilgour G, Rust AC, Tonini R (2017) Phreatic eruptions at
1185 crater lakes: occurrence statistics and probabilistic hazard forecast. J Appl Volcanol 6:4
1186 Tanaka R, Hashimoto T, Matsushima N, Ishido T (2018) Contention between supply of hydrothermal
1187 fluid and conduit obstruction: inferences from numerical simulations. Earth, Planets and
1188 Space 70(1):72.
1189 Thomas ME, Petford N, Bromhead EN (2004) The effect of internal gas pressurization on volcanic
1190 edifice stability: evolution towards a critical state. Terra Nova 16:312-317.
1191 Tsunematsu K, Ishimine Y, Kaneko T, Yoshimoto M, Fujii T, Yamaoka K (2016) Estimation of
1192 ballistic block landing energy during 2014 Mount Ontake eruption. Earth, Planets and Space
1193 68:88.
1194 Ventura G (1994) Tectonics, structural evolution and caldera formation on Vulcano Island (Aeolian
1195 Archipelago, southern Tyrrhenian Sea). J Volcanol Geotherm Res 60(3-4):207-224.
1196 Ventura G, Vilardo G, Milano G, Pino NA (1999) Relationships among crustal structure, volcanism
1197 and strike–slip tectonics in the Lipari–Vulcano volcanic complex (Aeolian Islands, Southern
1198 Tyrrhenian Sea, Italy). Phy Earth Plan Int 116(1-4):31-52.
1199 Voltaggio M, Barbieri M, Branca M, Castorina F, Taddeucci A, Tecce F, Tuccimei P, Turi B, Vesica P
1200 (1997) Calcite in fractures in a volcanic environment (Vulcano Island, Italy): contribution of
1201 geochronological and isotopic studies to volcanotectonics. J Volcanol Geotherm Res 75(3-
1202 4):271-282.
1203 Walker GP (1971) Grain-size characteristics of pyroclastic deposits. J Geol 79:696-714.
1204 Woods AW, Sparks RSJ, Ritchie LJ, Batey J, Gladstone C, Bursik MI (2002) The explosive

1205 decompression of a pressurized volcanic dome: the 26 December 1997 collapse and explosion
1206 of Soufrière Hills Volcano, Montserrat. Geol Soc London Mem 21:457-465.
1207 Yamamoto T, Nakamura Y, Glicken H (1999) Pyroclastic density current from the 1888 phreatic
1208 eruption of Bandai volcano, NE Japan. J Volcanol Geotherm Res 90:191–207.

Figure captions

Figure 1 – a) Geographic location and tectonic background of the Aeolian Archipelago. b) Digital Elevation Model (DEM) of the Lipari and Vulcano islands, highlighting the location of the recent (<55 ka) eruptive and tectonic activity (following Ruch et al. 2016). The location of the <2 ka eruptive vents are also reported. c) Map of the northern part of the Island of Vulcano. Main geographic features, location of the analysed stratigraphic natural sections and trenches are reported, with the inferred extent of the BdC deposits.

Figure 2 – (a) Synthetic log of the deposits related to the last 1000 years of eruptive activity at the La Fossa cone, modified after Di Traglia et al. (2013). The stratigraphic position of the Commenda lava is uncertain, and considered older (De Astis et al. 2013) or younger (Di Traglia et al. 2013) than the Palizzi/Campo Sportivo trachytic lavas. (b) Detailed stratigraphy of the deposits related to the Breccia di Commenda eruption. Labels for the different layers are explained in the main text. PCEC = Palizzi-Commenda Eruptive Cluster; PEU = Palizzi Eruptive Unit; CEU = Commenda Eruptive Unit; GCEC = Gran Cratere Eruptive Cluster.

Figure 3 – Detailed stratigraphy and correlations among key stratigraphic sections: in the horizontal axes FA = fine ash; CA = coarse ash; FL: fine lapilli; CL: coarse lapilli; B: bombs and blocks. Lithofacies symbols: a) cross-bedding; b) irregular-bedding; c) massive, unsorted; d) massive, well sorted; e) laminated; f) thinly laminated; g) massive, poorly sorted; h) fine-grained, unsorted; i) massive, fine-grained, well sorted; l) wavy-bedded; m) vesiculated; 1) mixed pumices-obsidian; 2) altered clasts; 3) banded clasts; 4) accretionary lapilli; 5) white/grey/golden pumices. Location of the sections is reported in Fig. 1.

Figure 4 – Dispersal and thickness variations for (a) Layers 1a and 1b; (b) Layers 2a; (c) Layer 2b and (d) Layer 2c. Thicknesses are in mm.

Figure 5 – Pictures of key outcrops for the BdC deposits. a) The most distal outcrops of Layer 2a (s153; refer to the electronic supplementary material for location), b) details of a), highlighting the stratigraphic and geometric relationship between Layer 2a and the Rocche Rosse tephra, as well as the coarse-grained and chaotic appearance of Layer 2a. The presence of contorted ash beds, derived from the erosion of the underlying deposits (Palizzi Eruptive Unit), are also emphasized and are related to ballistic impacts. c) impact structures at the base of Layer 2a in trenches in the south sector of the La Fossa cone (s148). d) the occurrence of the Layer 2b in the south-western part of the La Fossa cone (s71). e) massive lapilli tuff lithofacies in Layer 2c (above the Palizzi lava flow; Frazzetta et al. 1983; s27); f) accretionary lapilli rich lenses at the top of Layer 2c (s71).

Figure 6 – (a) Outcrop showing the thickest and coarsest breccia deposit (boulders up to 1.5 m diameter) related to Layer 2c, observed along the shoreline between Punte Nere and Porto di Levante bay (100 m south of section 5 in Fig. 7); (b) massive, boulder-rich (less than 1 m in diameter) Layer 2c breccia deposits in the Palizzi valley (section 21 in Fig. 7), showing rock fragments in the topmost part of the deposits derived from incorporation in the flow by bulking processes of Commenda lava clasts; (c) degassing pipes structures in Layer 2c (section 5 in Fig. 7). Tool for scale is 30 cm; (d) altered, oxidized, hard crust fragments within the most distal, southeast outcrop of Layer 2a (section 153 in Fig. 7). (e) Dense to vesicular, fresh and poorly altered lava clasts, containing mm-sized crystals of feldspar and pyroxene in fine-grained groundmass (section 5 in Fig. 7); (f) welded scoria clasts within Layer 2c close to the Porto di Levante area (section 5 in Fig. 7).

Figure 7 - Sampling site locations (in italics) and the results of the classification and relative abundances of different rock types, expressed as pie charts with percentage values. The dominant part of the material ejected during the BdC eruptive sequence consists of lava clasts with texture and composition similar to the trachytic lavas issued at the end of the Palizzi Eruptive Unit. Flow banded

1261 rhyolitic lavas (in orange) have been recognized only downslope of the rhyolitic Commenda lava.

1262

1263 Figure 8 – Grain-size features of BdC deposits, using both data from this work and from Gurioli et
1264 al. (2012). a) Mdφ vs σφ diagram (Walker 1971) and b) F1 vs F2 diagram (Walker 1971) of Layer 2a
1265 and Layer 2c, showing the lack of fines, as also observed in other fines-depleted, fines-poor and blast
1266 deposits (data from Boudon and Lajoie 1989; Brissette and Lajoie 1990; Yamamoto et al. 1999;
1267 Ritchie et al. 2002; Belousov et al. 2007; Lube et al. 2014; curves from Ritchie et al. 2002).

1268

1269 Figure 9 – Three-dimensional view of the eruption sequence after 3.5, 15, 20, 30, 40, and 50 seconds.
1270 Colour scale represents the logarithm in base 10 of the pyroclasts concentration (alpha), along a W-E
1271 section and at ground level. Ballistic particles of 8, 16 and 30 cm are drawn with different diameters
1272 and coloured depending on their velocity.

1273

1274 Figure 10 – Schematic reconstruction of the BdC eruption.

1275

1276 Figure C1. A) Computational domain and topographic surface used in 3D numerical simulations.
1277 Isolines are drawn every 25 m. B) Zoom of the fissure geometry. The topography is represented by a
1278 transparent grey surface, to show the excavated fissure. X Axis (red) is aligned West-East. Y Axis
1279 (yellow) is aligned South-North.

1280

1281
1282 **Table captions**

1283

1284 Table 1. Main phases and stratigraphic features of the deposits related to the Breccia di Commenda
1285 eruption. The summary of Gurioli et al. (2012) is also reported for comparison.

1286

1287 Table 2. Physical parameters of Layers 2a and 2c PDC deposits. A: Area; V: Volume; L: Length
1288 (measured following Hayashi and Self 1992); H: height (measured following Hayashi and Self 1992);
1289 λ: ratio of the average width to the length of an avalanche deposit (Dade and Huppert 1998); N_f:
1290 friction number ($A^{3/2}/\lambda^{1/2}\,V$; Dade and Huppert 1998).

1291

1292 Table 3. Geometric parameters and initial conditions of numerical simulations. Run names indicate
1293 Circular vents (C), Fissure (F) or Wedges (W). (*) indicates runs carried out with and without the
1294 added pressure gradient term in the Lagrangian equations. (**) indicate simulations with vent located
1295 NE of the present crater (as in Fig. 7). R is the fissure radius or half-width; L and B are the fissure
1296 length and depth, respectively; sh is the shape of the fissure (1=cone; 2=paraboloid; 1-10 indicates an
1297 asymmetric fissure); V is the fissure volume. Symbol ϕ_s denotes the solid particle fraction (i.e., 1
1298 minus the porosity of the exploding mass), n is the gas mass fraction, T the mixture temperature, P
1299 the initial pressure, M_s the total solid mass involved in the explosion, D indicates the distance reached
1300 by ballistic particles towards the East.

1301

1302 Table 4. Comparison between the Breccia di Commenda eruption and other hydrothermal eruptions.
1303 Data from Le Guern et al. (1980); Heiken et al. (1980); Sheridan (1980); Yamamoto et al. (1999);
1304 Lube et al. (2014); Breard et al. (2014, 2015); Kato et al. (2016); Maeno et al. (2016).

Figure 1

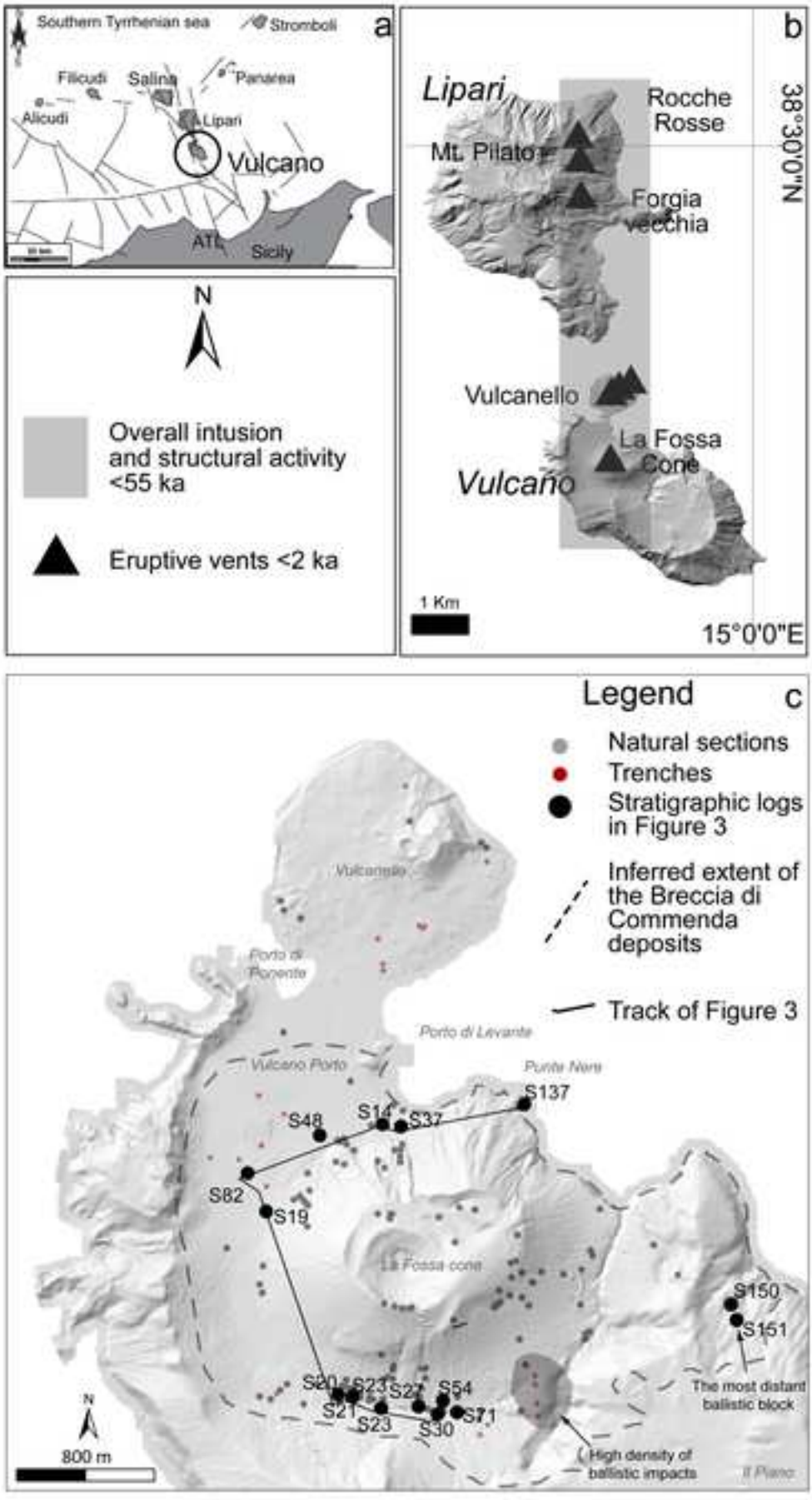

Figure 2

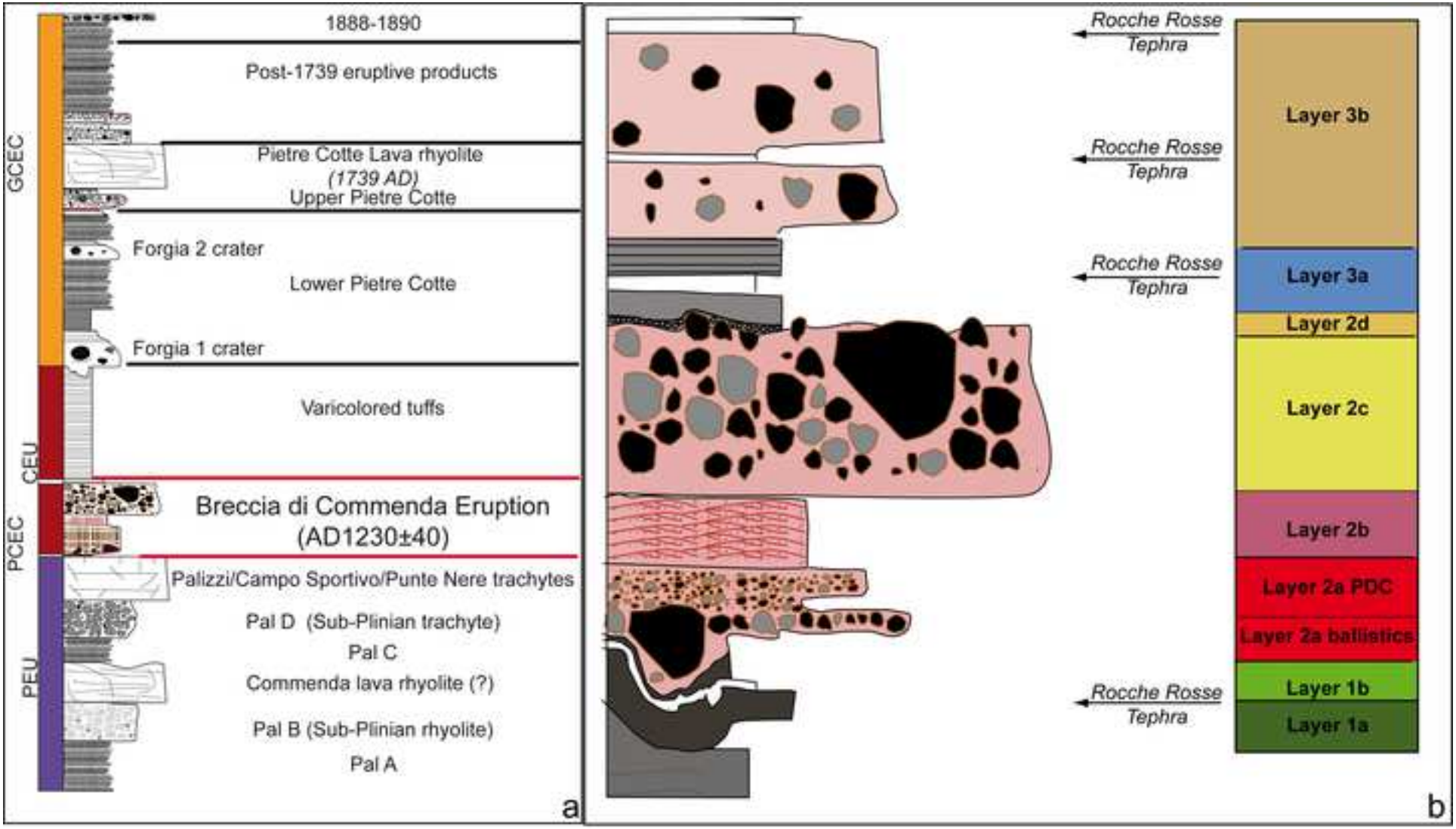

Figure 3

Click here to access/download;Figure;Figure 3.jpg

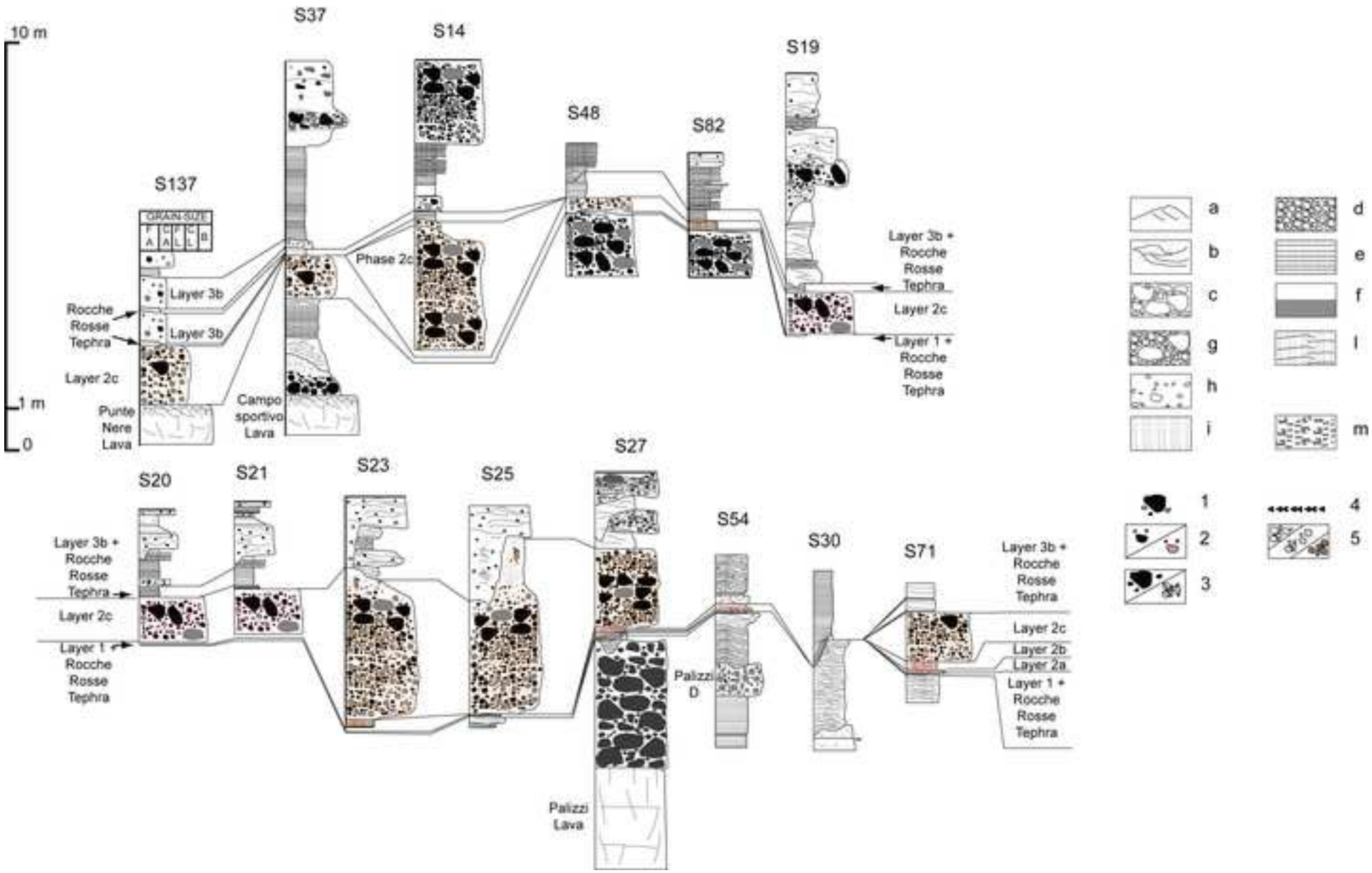

Figure 4

Click here to access/download;Figure;Figure 4.jpg

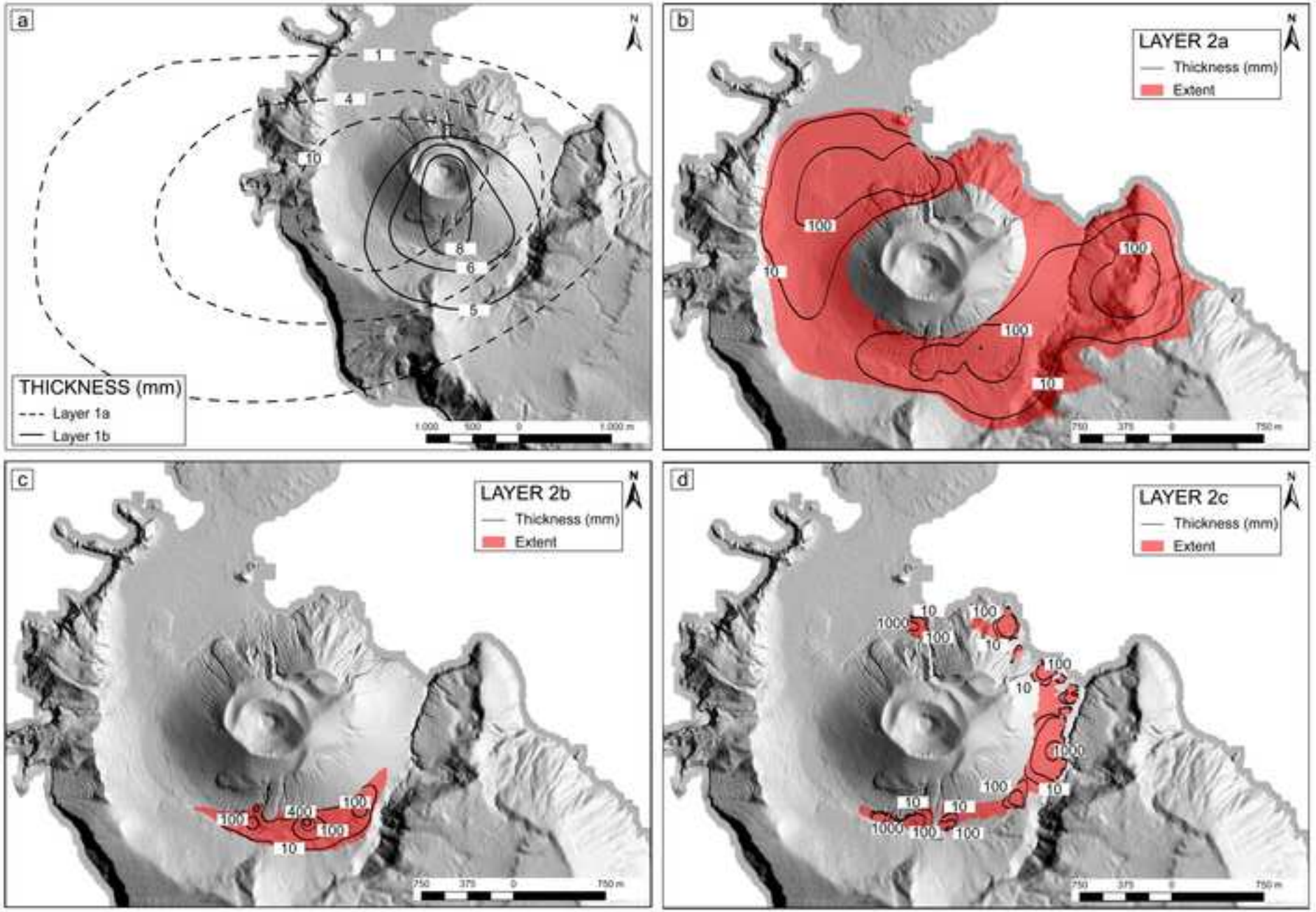

Figure 5

Click here to access/download;Figure;Figure 5.jpg

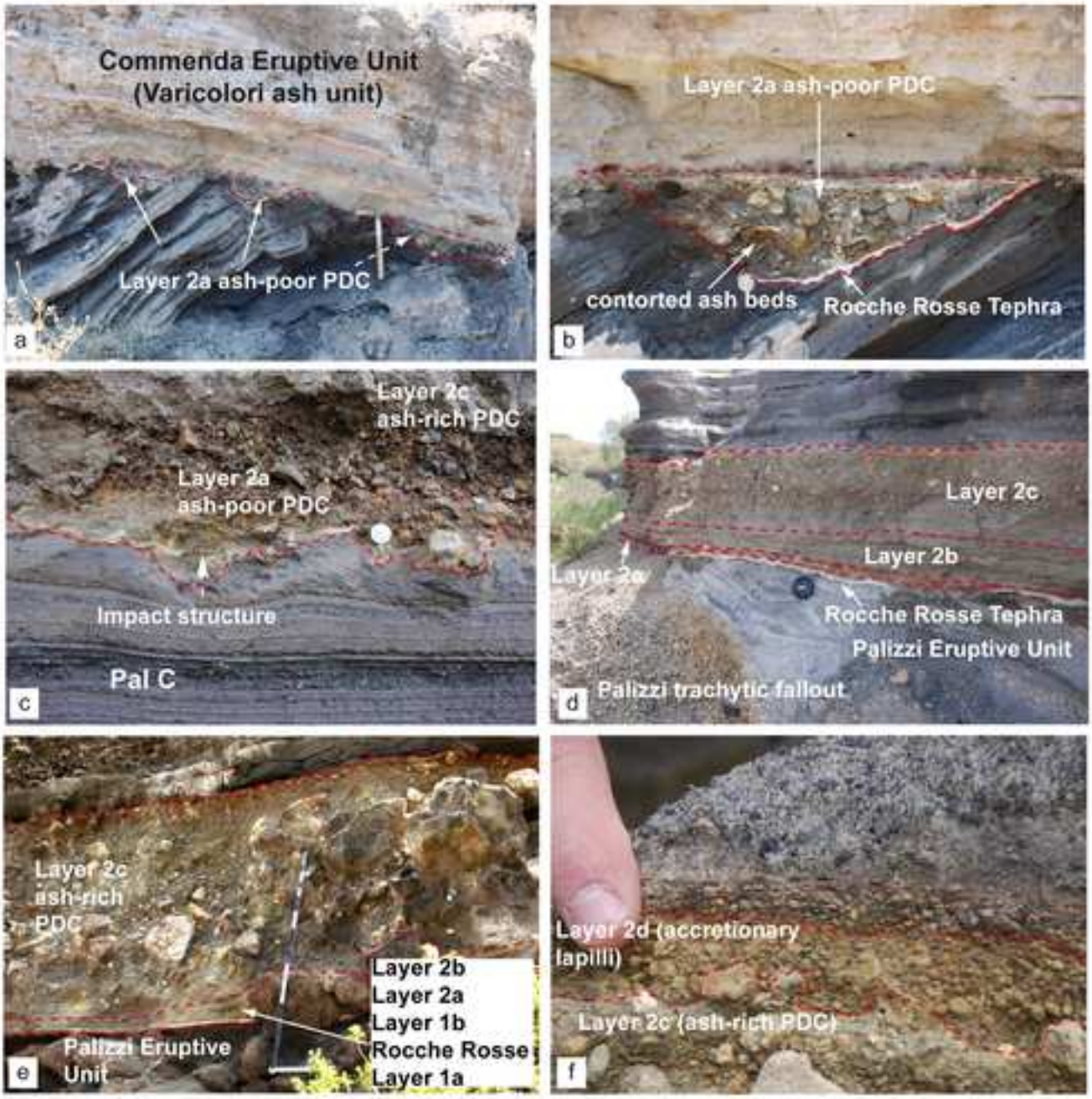

Figure 6

Click here to access/download;Figure;Figure 6.jpg

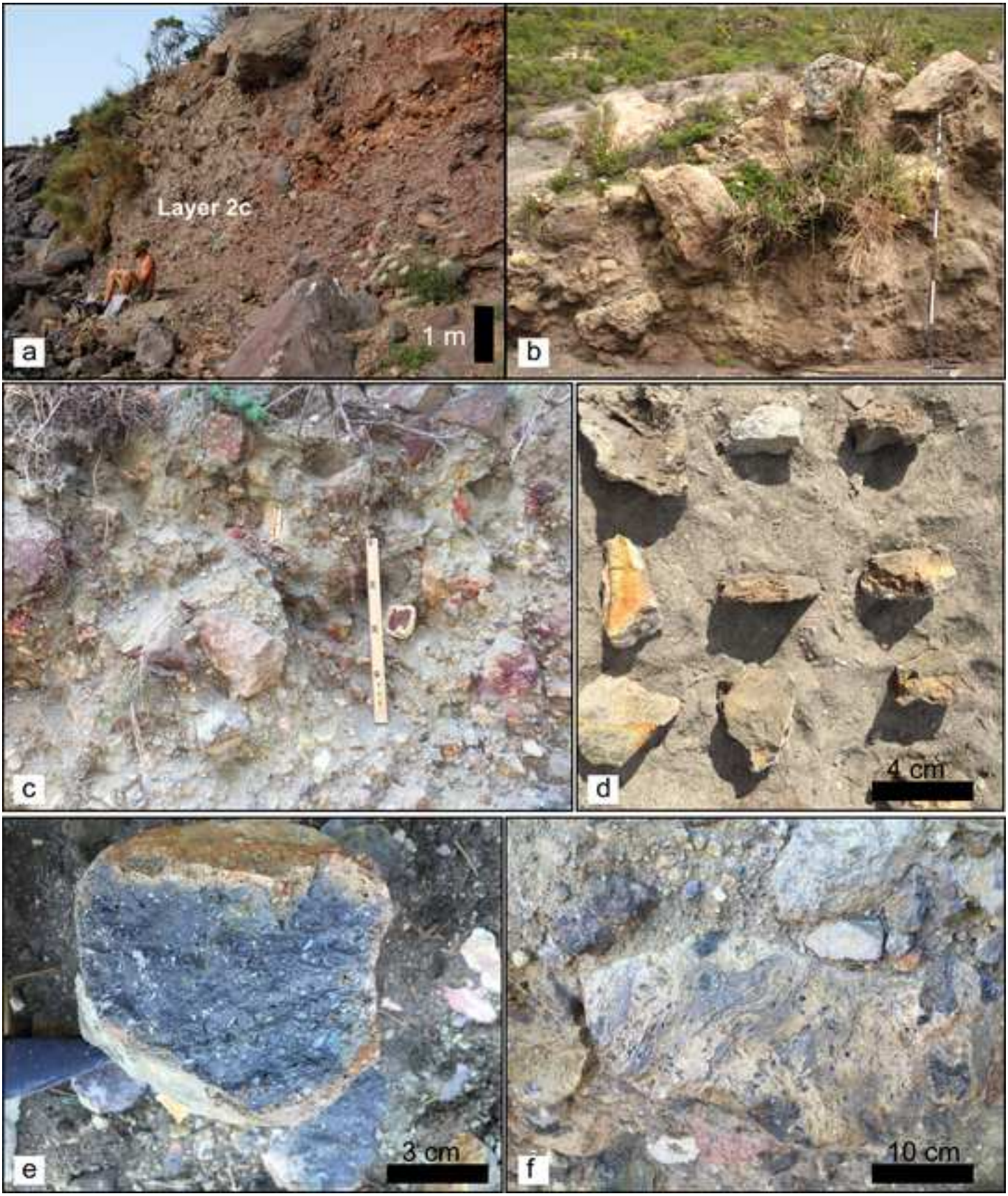

Figure 7

Click here to access/download;Figure;Figure 7.tif

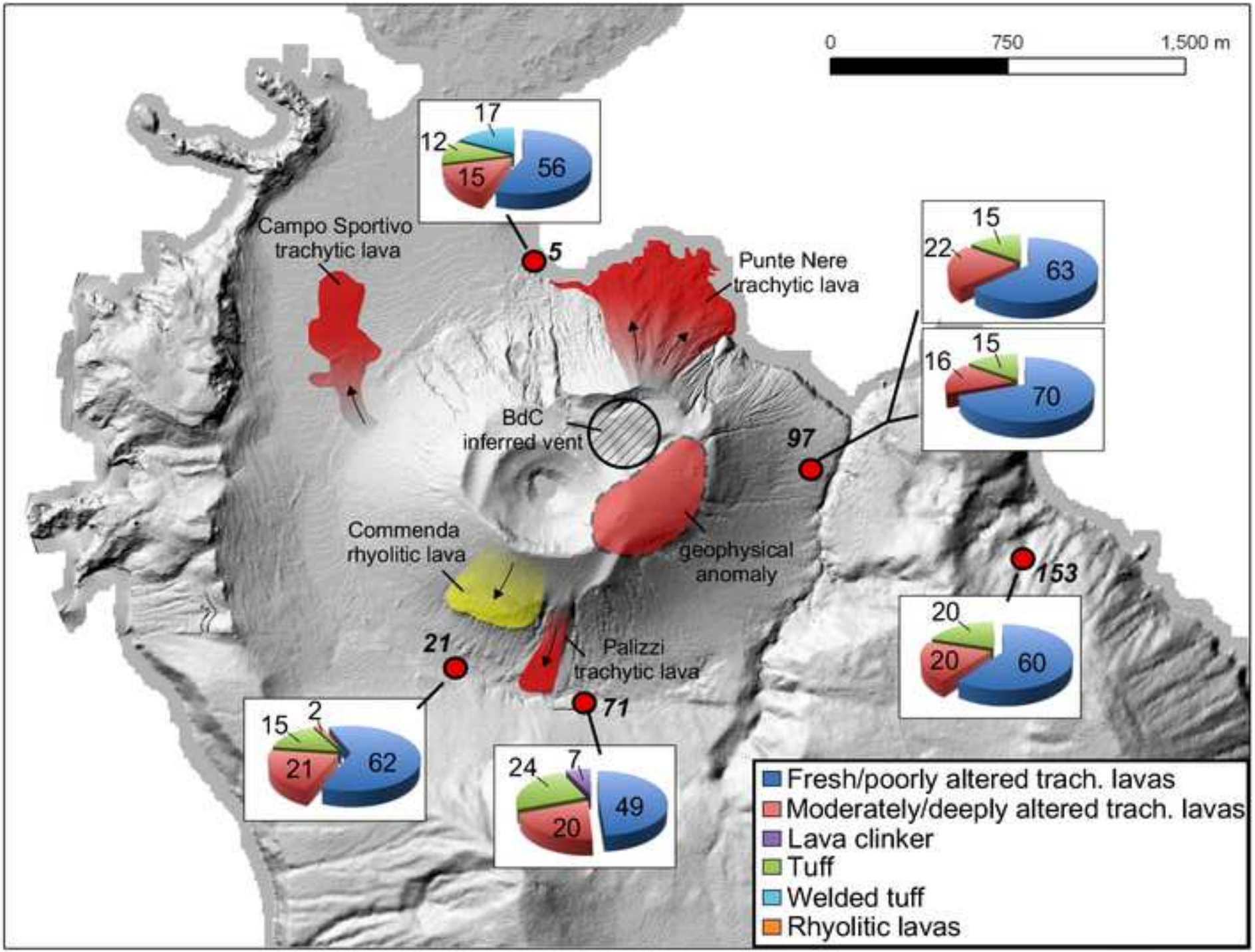

Figure 8

Click here to access/download;Figure;Figure 8.jpg

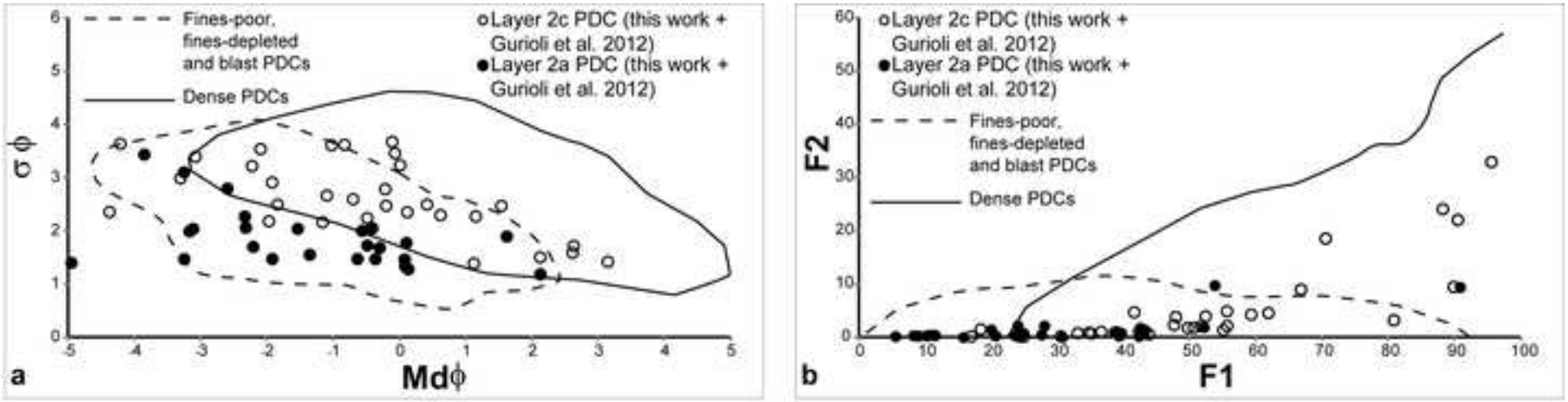

Figure 9

Click here to access/download;Figure;Figure 9.png

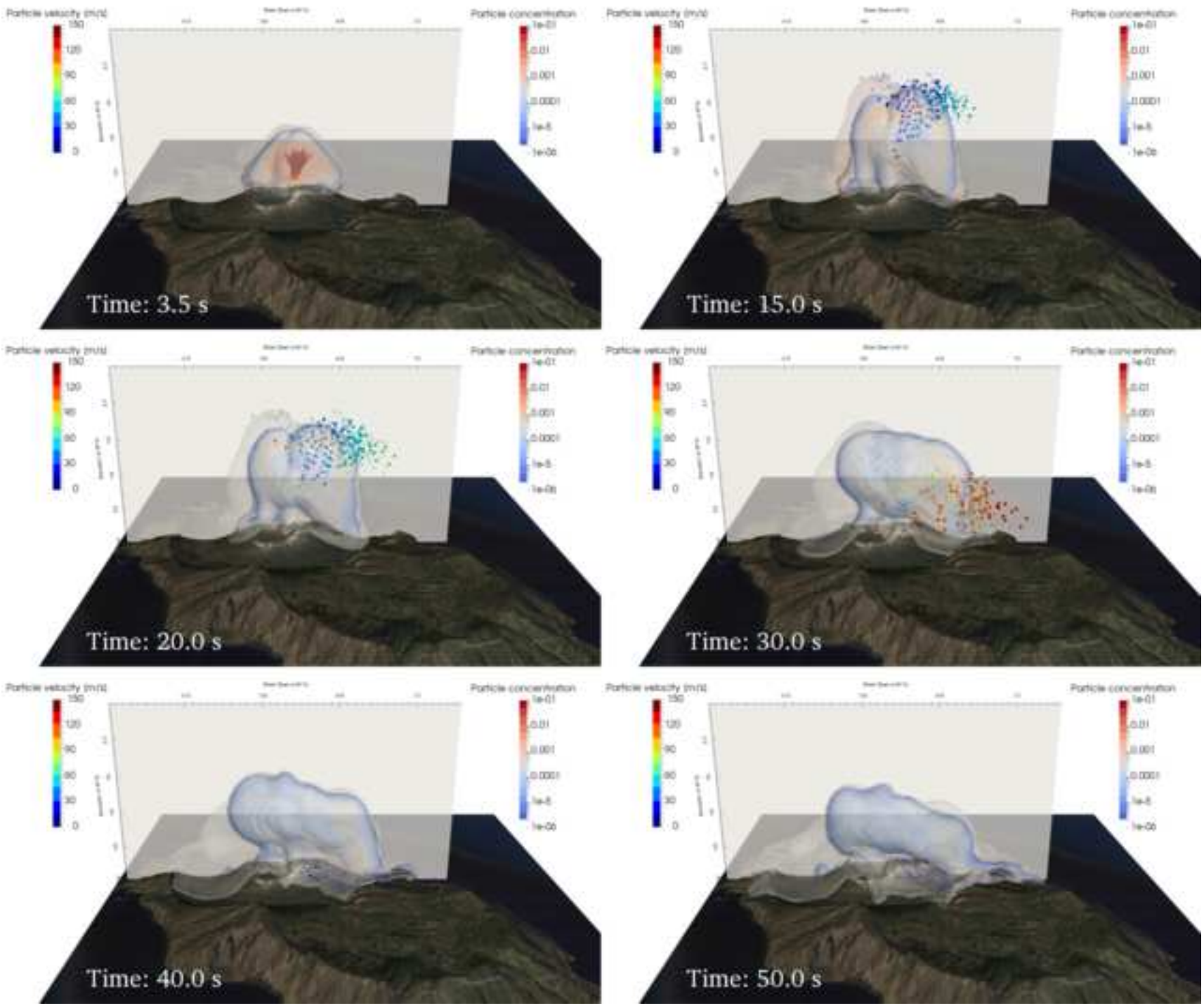

Figure 10

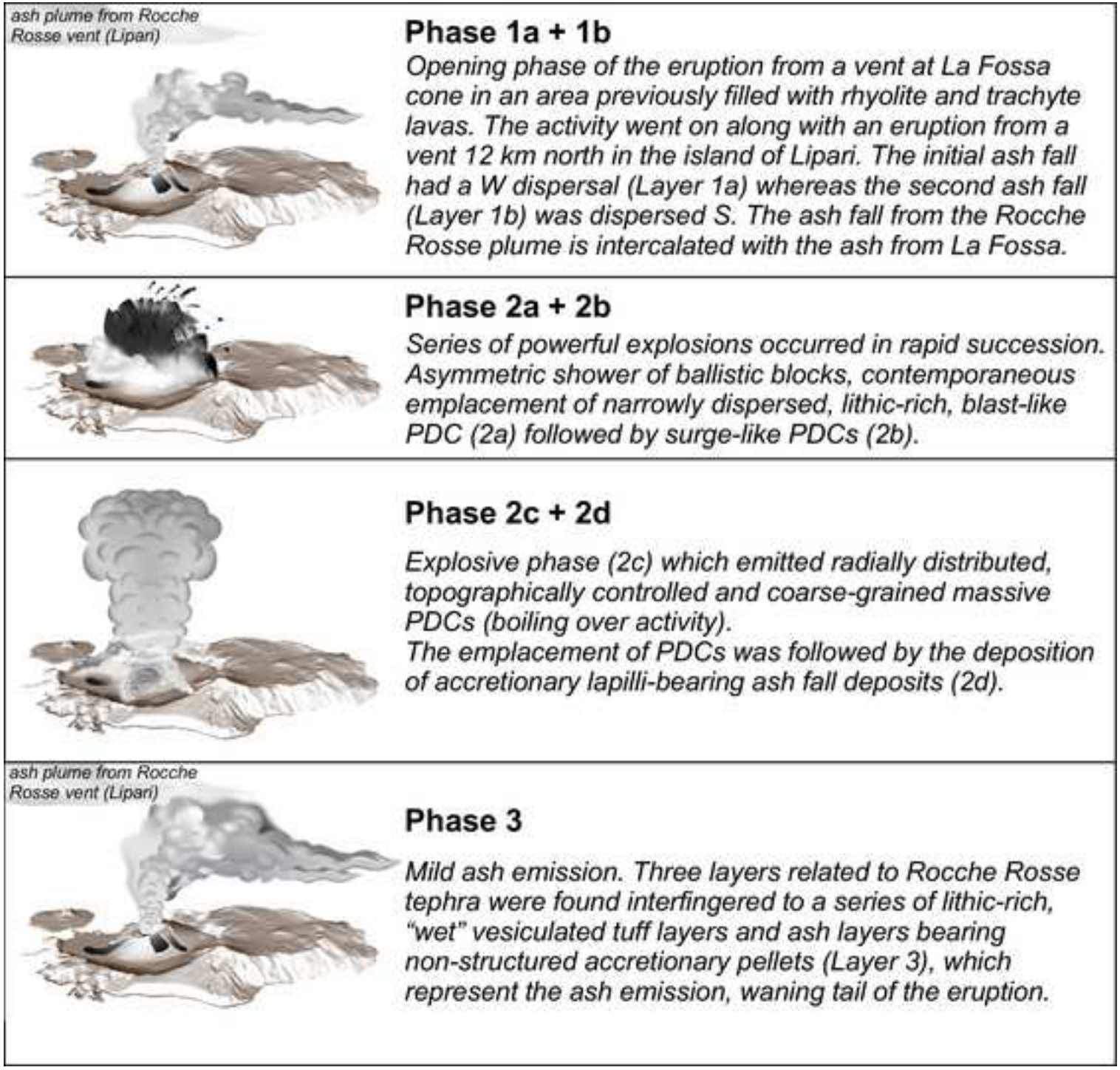

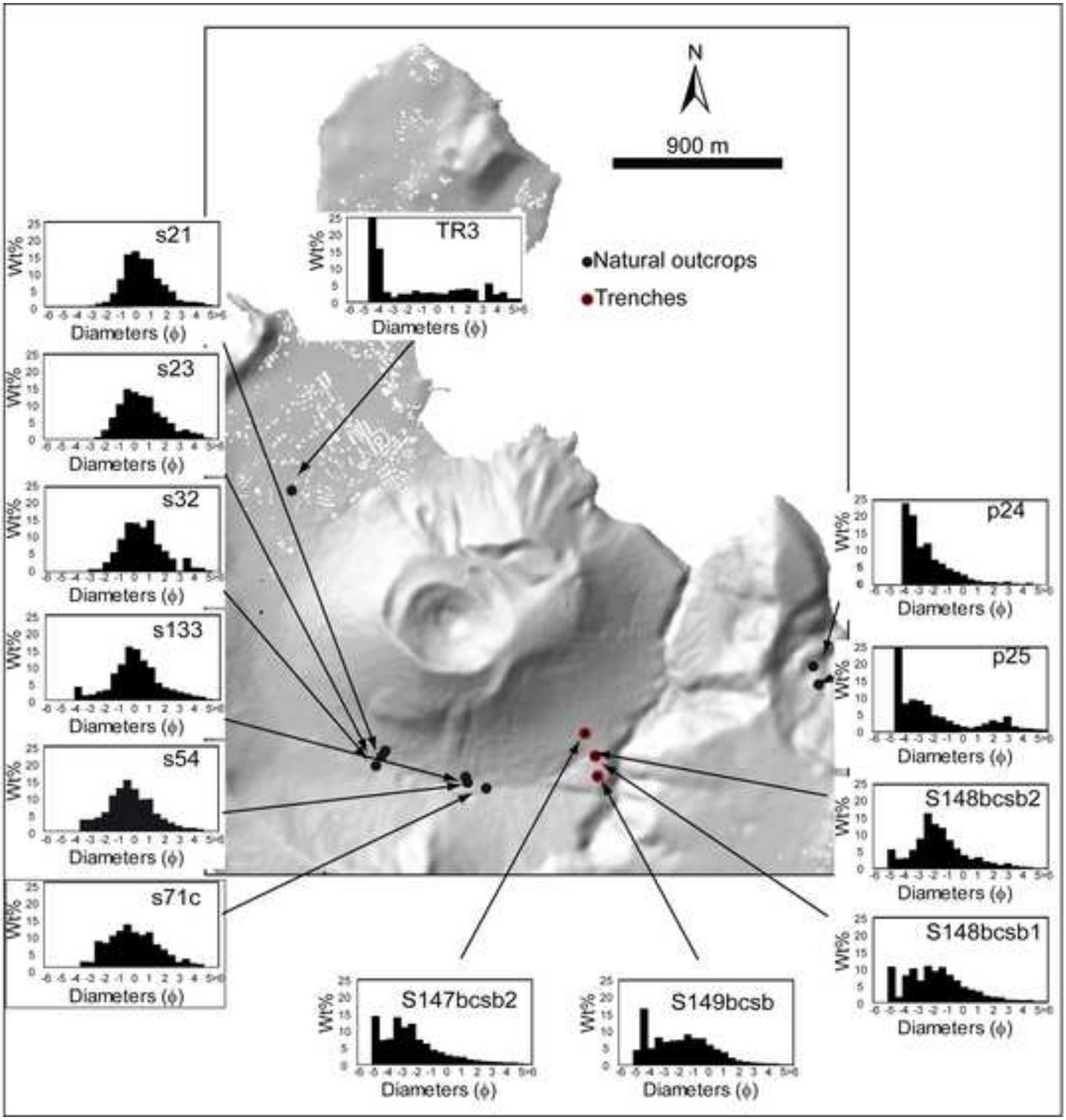

Table 1

Phases *Layers* *(Gurioli et al, 2012)*	**Phases** *(This work)*	**Layers** *(This work)*		***Description*** *(This work)*	
Phase 3 *Lithic ash fallout*	**Phase 3** *Final phase*	**Layer 3-rew** *Reworked deposit*	**Layer 3** *Lithic ash fallout*	**Layer 3-rew** **Lithofacies**: Massive, chaotic deposits. Sandy matrix with pebble and boulder-size clasts. Locally massive, chaotic, hardened, mud deposits. **Lithic clast type and shape**: Black-bluish, altered lavas, grey obsidian lavas; very altered, grey lavas; black, spherulitic obsidian lavas; very altered, black obsidian lavas, with grey flow-banding; black scoriae with red incrustation. The ash-matrix, if present, is red and constituted by altered clasts and crystals. Locally lithic mud. **Thickness and dispersion**: 10-100 cm. Northern and north-eastern cone-base. **Interpretation**: Reworked	**Layer 3** **Lithofacies**: parallel bedded, fine-ash layers. Each layer is massive. **Lithic clast type and shape**: Lithic ash. **Thickness**: 20-30 cm. **Other features**: Transition from accretionary lapilli-bearing to vesiculated tuffs layers. **Interpretation**: Lithic ash-fallouts.
Phase 2d *Lithic ash fallout*	**Phase 2d** *Lithic ash fallout*	**Phase 2d** *Lithic ash fallout*		**Lithofacies:** Massive, fine-ash lenses. **Lithic clast type and shape:** accretionary lapilli-bearing, brown-yellow, massive, well-sorted coarse ash. **Thickness and dispersion:** 5–10 cm. **Interpretation:** co-PDC deposits.	
Phase 2c *Dense PDC*	**Phase 2** *Paroxysmal phase*	**Layer 2c** Dense PDC		**Lithofacies**: Massive, chaotic, block-and-ash deposit (~5° slope angle). Fines-poor pipes (major valleys). Large boulder-size clasts (break in slope). **Lithic clast type and shape**: Black-bluish, altered lavas, grey obsidian lavas; very altered, grey lavas; black, spherulitic obsidian lavas; very altered, black obsidian lavas, with grey flow-banding; black scoriae with red incrustation. The ash-matrix, if present, is red and constituted by altered clasts and crystals. **Thickness and dispersion**: Up to 345 cm. Radial. **Other features**: Up to 1 m sub-rounded blocks with extensive external alteration. Absence of thermal contraction.	

			Interpretation: Dense PDC. Fluid escape dominated flow-boundary zone, turbulent shear induced tractional segregation. Major valleys: pipes due to vapour flashing in wet environment. Break in slope: localized current non-uniformity (depletive competence).
Phase 2b *Dilute PDC*		**Layer 2b** Dilute PDC	**Lithofacies**: sequence of fines-poor and fines-rich cross-bedded, normal graded laminae. **Lithic clast type and shape**: Black-bluish, altered lavas, grey obsidian lavas; very altered, grey lavas; black, spherulitic obsidian lavas; very altered, black obsidian lavas, with grey flow-banding; black scoriae with red incrustation. The ash-matrix, if present, is red and constituted by altered clasts and crystals. **Thickness and dispersion**: Up to 50 cm. South-ward dispersion. **Interpretation**: Dilute PDCs.
Phase 2a *Ballistics + dilute PDC*		**Layer 2a** Ballistics + diluted PDCs	**Lithofacies**: (*Basal lenses*) Coarse-grained and fines-poor, discontinuous lenses or layers of coarse lapilli to boulder-size clasts; (*main deposit*) Fines-poor, normal-to-reverse graded, clast-supported, continuous layer or discontinuous lenses. Diffuse-stratified, thin-bedded, not laterally persistent, low-angle truncations (small irregularities). Fines-poor, clast-supported, discontinuous lenses (large irregularities). **Lithic clast type and shape**: Black-bluish, altered lavas, grey obsidian lavas; very altered, grey lavas; black, spherulitic obsidian lavas; very altered, black obsidian lavas, with grey flow-banding; black scoriae with red incrustation. The ash-matrix, if present, is red and constituted by altered clasts and crystals. **Thickness and dispersion:** (*Basal lenses*) Up to 30 cm diameter-clast. Radial, southeastern-ward dispersion; (*main deposit*) Up to 100 cm. Radial, south-ward and eastern-ward dispersion. **Interpretation:** (*Basal lenses*) balistics; (*main deposit*) Dilute PDC Main facies: high deposition rate Small-irregularities: subtle unsteadiness Large irregularities: reduction of flow competence due to “blocking-effect”.
Phase 1 *Lithic ash fallout*	**Phase 1** *Opening phase*	**Layer 1b** Lithic ash fallout	**Lithofacies:** Massive, fine-ash layer. **Lithic clast type and shape:** Lithic ash. **Thickness and dispersion:** 5 to 8 cm. South-ward dispersion. **Other features:** S-bearing incrustations. **Interpretation:** Lithic ash-fallout.
		Layer 1a Lithic ash fallout	**Lithofacies:** Massive, fine-ash layer. **Lithic clast type and shape:** Lithic ash.

			Thickness and dispersion: 1 to 10 cm. West-ward dispersion. **Other features:** S-bearing incrustations. **Interpretation:** Lithic ash-fallout.

Table 1

Table 2

Parameters	**Layer 2a**	**Layer 2c**
A (km^2)	4.68	0.44
V ($x\ 10^6\ m^3$)	2.71	1.39
L (km)	1.7	1.28
H (km)	0.38	0.38
H/L	0.224	2.97
λ	1.62	0.271
$A/V^{2/3}$	668	216
N_f	2.93×10^4	4.08×10^3

Table 3

Run	Geometry					Mixture properties					Collapse	Ballistic range
	R [m]	L [m]	B [m]	sh	V [m^3]	ϕ_s	n %	T [K]	P [MPa]	M_s [kg]		D [km]
C1*	100		200	1	2.0e06	0.3	7.5	523	12.0	1.5e09	Full	[1.15; 1.40; 1.65]
C2*	100		200	1	2.0e06	0.3	5.8	673	12.0	1.5e09	Full	[1.25; 1.45; 1.65]
C3*	67		268	2	1.6e06	0.3	7.5	523	12.0	1.0e09	Minor	Exit top boundary
C4	67		268	2	1.6e06	0.6	1.8	523	12.0	1.9e09	Partial	Exit top boundary
F-N45E*	40	200	160	1-10	2.1e06	0.3	7.5	523	12.0	1.6e09	Full (asymmetric)	[1.45; 1.70; 1.95]
F-N35E**	40	200	160	1-10	1.9e06	0.3	7.5	523	12.0	1.4e09	Full (asymmetric)	[1.25; 1.70; 2.00]
W1*	40	200	160	2	2.4e06	0.3	7.5	523	12.0	1.8e09	Partial (E-W)	[1.40; 1.70; 1.90]
W2	40	200	160	2	1.6e06	0.3	6.3	623	12.0	1.2e09	Partial (E-W)	[1.45; 1.70; 1.90]
W3	40	200	160	2	2.5e06	0.5	3.2	523	12.0	3.1e09	Full	[1.40; 1.10; 1.20]

Table 4.

Table 4

	Fossa cone (13th century AD Breccia di Commenda)	***Bandai (1888)***	***Adatara (1900)***	***Zao (1895)***	***Soufrière de Guadeloupe (1975-1977)***	***Te Maari (6 August 2012)***	***Ontake (27 September 2014)***
Dormancy period (years)	?	101	1	4	10	84	7
Trigger	Input of magmatic gas due to deep mafic injection	Depressurization of the hydrothermal system	Thermal energy of hydrothermal fluids	Shallow intrusion	Input of magmatic gas due dike injection/shallow intrusion	Depressurization of the hydrothermal system	Depressurization of the hydrothermal system
Pre-blast phase							
Duration	?	0	1 year	1 year	1 year	1 month	0
	Ash-explosions	No pre-climactic phase	Increase fumaroles discharge; slight quakes; ash explosions	Increase fumaroles discharge; ash explosions	Seismic activity; increase fumaroles discharge; Steam explosions, ash explosions	Increased seismic and hydrothermal activity commenced a month before the eruption. Strong increase in late July 2012	A seismic swarm occurred during 6-7 days before but declined over the following days. The frequency of volcano tectonic (VT) earthquakes gradually increased 11 days and peaked on 6 before the eruption
Blast phase							
Duration	?	20 min	7.30 hours	?	48 min	6-7 min	3-6 min
Number of events	3 (at least)	More than 20	5 (the last was the most energetic)	1	1	6 events. ≈95% of the energy was released during four distinct pulses of explosions within the initial 20 s	3 events lasted 23 min

Directed vs radial	Initial directed ballistic and radial PDC, then directed PDCs and radial PDC	Directed	Radial	Radial	Directed	Initial directed ballistics and PDCs, then radial PDCs	Three main branches
Maximum travel distance	> 2.2 km	Up to 6 km	Up to 2.4 km	< 0.5 km	3.5 km	2.5 km	Max 2.4 km
Area affected by PDCs	Up to 4.6 km^2	13 km^2				6.1 km^2	
Volume of PDCs deposits	2.9×10^{-4} km^3	10^{-3} km^3	2.8×10^{-4} km^3	10^{-6} km^3	6×10^{-4} km^3	3.4×10^{-4} km^3	$4\text{-}7\times10^{-4}$ km^3
Range of ballistic-ejection	Up to 2,2 km	?	?	?	Hundreds of meters	> 2 km (covered area: $5{,}1\times10^6$ m^2)	
Amount of juvenile material	?	0	0	0	0	0	0

Table 5